Balanced proper-orthogonal-decomposition-based feedback control of vortex-induced vibration

Haokui Jiang ⬥ and Shunxiang Cao ⬥*
Institute for Ocean Engineering, Shenzhen International Graduate School,
Tsinghua University, Shenzhen 518055, China

This work develops a reduced-order model-based feedback control strategy for suppressing vortex-induced vibration (VIV) of a spring-mounted cylinder. First, a reduced-order model (ROM) is constructed for the cylinder flow using the balanced proper orthogonal decomposition (BPOD) method. The BPOD model employs a projection-free snapshot-based approach, demonstrating a close agreement with the full-order model (FOM). Then, the ROM is applied to design an active flow control strategy that utilizes blowing and suction actuators attached to the cylinder to suppress the VIV within the FOM framework. By employing the linear-quadratic Gaussian, optimal control strategies are derived, which effectively suppresses VIV within the Reynolds number range up to Re = 100. Both model-based prediction and actual controlled performance show that the controller suppresses vibration by adjusting or eliminating those unstable eigenmodes. This control mechanism transforms the flow dynamics into either modified inherent eigenmodes or new modes. The former occurs when inherent eigenmodes closely align with the zero growth rate plane. For the latter, however, additional energy is required to sustain the newly induced modes, which impedes the suppression process. Furthermore, we find that positioning velocity probes in close proximity to $x/D = 3.0$ yields a significant gain margin across various Reynolds numbers while adhering to the controllability conditions. This indicates that the placement of probes in wavemaker regions can be suboptimal. Finally, the obtained optimal control strategies exhibit robustness in the presence of considerable variations in Reynolds numbers.

I. INTRODUCTION

The phenomenon of vortex-induced vibration (VIV) [1] is common in flexible cylindrical structures immersed in fluids, such as suspended cables [2] and offshore risers [3]. A vortex street can potentially occur at Reynolds number Re as low as 20, exerting cross-flow perturbation forces on the structure and triggering self-excited oscillation [4,5]. VIV can lead to the rapid accumulation of fatigue damage or the sudden collapse of the structure, causing catastrophic failures in marine structures [6,7]. Hence, the control of VIV has been the focus of substantial research efforts. Recently, Wang *et al.* developed active control techniques that use blowing and suction actuators to control the wake instability and effectively suppressed VIV at Re = 100 [8]. They employed proportional-integral control schemes to dynamically adjust jet velocity based on the flow information extracted from probes. More recently, Raissi *et al.* [9] and Zheng *et al.* [10] developed deep reinforcement learning (DRL)-based active flow control (AFC) to suppress VIV at Re = 100.

---

*Contact author: caoshunxiang@sz.tsinghua.edu.cn

Despite achieving certain degrees of success, these control strategies are developed based on the full-order model (FOM), presenting a demand for substantial computation time.

Compared to directly controlling the FOM, devising optimal control strategies through reduced-order models (ROMs) and subsequently applying them to control FOMs is a more efficient approach. This is because ROMs can utilize well-developed, efficient, and robust control design tools [11]. Hence, the objective of this work is to develop a closed-loop AFC algorithm using the balanced proper orthogonal decomposition (BPOD) ROM to stabilize the wake flow and suppress the VIV. In this context, we focus on controlling a two-dimensional (2D) spring-mounted cylinder with one degree of freedom (1DOF) along the normal direction. The control strategy involves manipulating jets generated by a pair of blowing and suction actuators attached to the cylinder.

To construct the ROM, the system identification and the BPOD-based approach are two widely used model reduction techniques [12]. The former constructs ROMs relying solely on information collected by probes and actuators [13], which are known as black-box models, including well-developed techniques such as the eigensystem realization algorithm (ERA) [14–16] and the autoregressive method (ARX) [5]. Several studies have applied these black-box ROMs in the design of a controller for VIV. For example, Yao and Jaiman designed a linear-quadratic regulator (LQR) controller based on an ERA-based ROM to control VIV at Re = 60 [17]. Cheng *et al.* [18] conducted a study on the impact of the windward interior angles of elastically mounted trapezoidal bodies on a galloping instability at Re = 160. Luo *et al.* developed an ARX-based ROM and suppressed VIV by actively controlling a tuned mass damper (TMD) at Re = 60 [19]. However, the black-box models have inherent limitations, such as lack of physical interpretability and limited extrapolation, and might not provide the necessary information for designing effective control strategies.

The BPOD-based ROM is a grey-box model that characterizes the dominant controllability and observability of coherent structures through an approximate balanced truncation method [20]. Compared to the black-box model, it offers the advantage of accurately capturing dynamics in non-normal systems [21] and identifying structural characteristics of modes that are crucial to control. Hence, it provides a more comprehensive understanding of the intricate mechanism behind complex fluid-structure interaction (FSI) problems and has demonstrated successful application in feedback control [22–24]. This work aims at pioneering the application of BPOD ROM in the VIV control, harnessing its unique capability of incorporating additional physical mechanisms for guiding optimal control strategies [25]. We also provide an alternative perspective for elucidating control mechanisms through the analysis of eigenfunctions.

Constructing the BPOD model for FSI problems require solving the linear direct and adjoint equations governing the coupled fluid-structure dynamics. This process introduces intrinsic theoretical complexities in modeling [26], particularly in regard to the coupling of fluid and structural systems. Lesoinne *et al.* formulated the linear FSI problem by treating the grid velocity as a pseudovariable within the framework of arbitrary Eulerian-Lagrangian (ALE) formulation [27]. Within the ALE framework, further advancements have been achieved in the linear direct and adjoint modeling of FSI systems [28–30]. However, difficulty arises in the linearization process due to the Lagrangian motion of the fluid-structure interface [30]. In addition to the ALE method, Goza *et al.* performed a global linear instability analysis (LSA) within the immersed boundary method (IBM) framework to study the VIV in the inverted flag flapping [31]. IBM also presents challenges when it comes to efficiently handling interface constraint [32,33]. The recently developed linearized lattice Boltzmann method (LLBM) can deal with interfaces efficiently, but it is difficult to recover a macroscopic linear adjoint equation from Chapman-Enskog analysis [34,35]. Beyond these general methods, there are specialized methods designed for modeling rigid structural motion problems and overcoming the above challenges. Basso *et al.* applied a time-varying coordinate mapping technology to couple the fluid and rotationally structural systems for LSA and sensitivity analysis [36]. Tchoufag *et al.* and Sabino *et al.* conducted LSA by formulating the fluid governing equations in a non-inertial frame of reference. This involved formulating the linear equation by

constructing the absolute velocity within the frame of reference that moves along with the structure [37,38]. We employ this approach and further derive the linear adjoint equation of the VIV system to construct the BPOD model.

With the solution of the adjoint equation, the BPOD-based method possesses an additional advantage—namely, the capability to incorporate physical mechanisms into the arrangement of actuators and probes, which facilitates the optimal probe placement. In the literature, it is a common practice to place probes within the wavemaker region, i.e., the region with high structural sensitivity, as it can identify locations with both a high sensitivity and a strong response of the leading unstable mode (modes with the largest growth rate) [39]. Åkervik *et al.* strategically placed actuators and probes across the wavemaker region, achieving good detectability and stabilizability in controlling separated boundary-layer flow [40]. Flinois and Morgans similarly chose this region for actuator and probe placement when using the ERA to control the unstable flow around a D-shaped body [41]. Li and Zhang found that placing the probes to cover the wavemaker region is a key factor in successful vortex suppression through reinforcement learning (RL) for the stationary cylinder case [42]. For the control of FSI systems, placements of either force probes or velocity probes are typically determined through empirical knowledge. Yao and Jaiman strategically placed force probes across the wavemaker region determined from the stationary cylinder case, achieving successful control of the VIV [17]. However, the wavemaker region is not always the optimal location for actuators or probes in the context of the Ginzburg-Landau system [43,44]. Similarly, Jin *et al.* observed that, in the context of cylinder flow, the wavemaker region does not carry significant importance for the optimal placement of actuators and sensors [11]. Therefore, whether placing probes across the wavemaker region determined by the leading direct and adjoint eigenmode is optimal for the VIV system requires further validation. In this regard, we compare the spatial distribution of high structural sensitivity and robustness across different probe locations.

To quantify the control robustness, a linear-quadratic Gaussian (LQG) framework is employed, which has been utilized in numerous studies [45–47]. The LQG controller consists of the design of a dynamic observer and a Kalman filter, which provide optimal state estimation for the system [48]. Gain margins (GMs) are used to quantitatively measure the stability robustness [49]. Unlike machine-learning-based methods, this model-based controller does not necessitate extensive training time and boasts remarkable robustness. Sipp and Schmid successfully implemented a robust LQG controller to manage the scenario at $Re = 7000$ using a strategy initially designed for $Re = 7500$ in open cavity flow [50]. Similar studies can be found in Refs. [17,51]. By integrating a physical mechanism with the optimal placement of actuators and probes, we expect the development of a highly robust controller capable of effectively controlling VIV across a broad range of Reynolds numbers and other relevant physical parameters.

The paper is organized as follows: In Sec. II, we outline the physics problem under investigation, including the governing equations, the formulation of the linear direct and adjoint equations, and the BPOD ROM for unstable flows. Section III presents the numerical schemes and the verifications. Section IV presents the global linear instability analysis, BPOD modeling of VIV, analysis of control performance, and the discussion about control robustness on actuator and probe placement. Lastly, concluding remarks are provided in Sec. V.

II. PROBLEM FORMULATION

A. Problem definition

We consider a 2D spring-mounted cylinder in an open flow [Fig. 1(a)]. A 2D Cartesian coordinate system with its origin at the center of the cylinder is used, which travels with the cylinder's motion. The x coordinate aligns with the streamwise direction, whereas the y coordinate corresponds to the lateral direction. The cylinder's motion is restricted along the lateral direction. Following the formulation by Mougin and Magnaudet [52], we express the absolute velocity $\boldsymbol{u}$ within a reference frame that moves with the cylinder. The flow around the cylinder can be described by
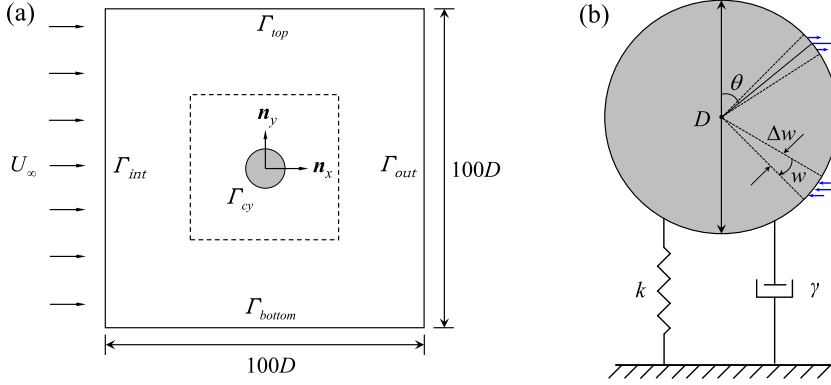
FIG. 1. (a) Schematic depiction of the computational domain and boundary conditions. (b) Schematic showing the damped spring-mass cylinder and the control actuators.

the nondimensional incompressible Navier-Stokes equations,

$$\nabla \cdot \boldsymbol{u} = 0, \tag{1}$$

$$\frac{\partial \boldsymbol{u}}{\partial t} + [(\boldsymbol{u} - \zeta \boldsymbol{n}_y) \cdot \nabla]\boldsymbol{u} + \nabla p - \frac{1}{\text{Re}}\nabla^2 \boldsymbol{u} = 0, \tag{2}$$

where $\boldsymbol{u} = (u_x, u_y)$ is the velocity, p is the pressure, ζ represents the velocity of the cylinder, and $\boldsymbol{n}$ is the direction vector. The equations governing the motion of the cylinder are formulated as follows:

$$\frac{\partial \eta}{\partial t} - \zeta = 0, \tag{3}$$

$$\frac{\partial \zeta}{\partial t} - \xi = 0, \tag{4}$$

$$\xi + \frac{4\pi\gamma}{U^*}\zeta + \left(\frac{2\pi}{U^*}\right)^2 \eta - \frac{2C_y}{\pi m} = 0, \tag{5}$$

where η, ζ, and ξ represent the displacement away from the origin, the velocity, and the acceleration of the cylinder, respectively; γ is the damping ratio, and in this study it is assumed to be zero. Other dimensionless parameters are given by

$$m = \frac{\rho_c}{\rho_f}, \quad U^* = \frac{2\pi U_\infty \sqrt{m_c/k}}{D},$$

$$\text{Re} = \frac{DU_\infty}{\nu}, \quad C_y = \frac{2[\boldsymbol{F}_p(p) + \boldsymbol{F}_u(\boldsymbol{u})]}{U_\infty^2 D}, \tag{6}$$

where $D = 1$ is the diameter of the cylinder, $U_\infty = 1$ is the upstream unperturbed velocity, ν is the kinematic viscosity, m is the mass ratio between the cylinder ρ_c and fluid densities ρ_f, U^* is the reduced velocity, m_c is the cylinder mass, k is the spring stiffness, Re is the Reynolds number, C_y is the vertical force coefficient, and $\boldsymbol{F}_p$ and $\boldsymbol{F}_u$ represent the linear force operators, which are calculated as follows:

$$\boldsymbol{F}_p(p) = \int_{\Gamma_{cy}} (-p\boldsymbol{I}) \cdot \boldsymbol{n}_y d\Gamma,$$

$$\boldsymbol{F}_u(\boldsymbol{u}) = \int_{\Gamma_{cy}} \frac{1}{\text{Re}}[\nabla \boldsymbol{u} + (\nabla \boldsymbol{u})^T] \cdot \boldsymbol{n}_y d\Gamma, \tag{7}$$

where $\boldsymbol{I}$ is the unit matrix. For direct numerical simulation (DNS), the boundary conditions are given as

$$\boldsymbol{u} = -\zeta\boldsymbol{n}_y \quad \text{on } \Gamma_{cy}, \tag{8}$$

$$\boldsymbol{u} = U_\infty\boldsymbol{n}_x \quad \text{on } \Gamma_{\text{int}} \cup \Gamma_{\text{top}} \cup \Gamma_{\text{bottom}}, \tag{9}$$

$$\left[-\boldsymbol{\nabla}p + \frac{1}{\text{Re}}(\boldsymbol{\nabla}\boldsymbol{u} + (\boldsymbol{\nabla}\boldsymbol{u})^T)\right]\cdot\boldsymbol{n} = 0 \quad \text{on } \Gamma_{\text{out}}. \tag{10}$$

As shown in Fig. 1(b), the control actuators consist of a pair of blowing and suction jets symmetrically positioned along the x axis, at an angle of θ with respect to the y axis. Each jet has a width of $\Delta w = \pi/10$ and flows horizontally at its outlet. For both jets, a velocity boundary condition of a sinelike profile is applied:

$$\boldsymbol{u}_{\text{upper}} = (u_x, 0)^T = Q_{\text{upper}}\sin\left(\frac{w\pi}{\Delta w}\right),$$

$$\boldsymbol{u}_{\text{lower}} = (u_x, 0)^T = Q_{\text{lower}}\sin\left(\frac{w\pi}{\Delta w}\right), \tag{11}$$

where w is the radian angular coordinate along the clockwise direction on the surface of jets. The flow rates of the upper and lower jets are controlled by changing the scalar values of Q_{upper} and Q_{lower}, respectively. The condition $Q_{\text{upper}} + Q_{\text{lower}} = 0$ is enforced to ensure that there is no additional mass added to the flow.

B. Formulation of the linear direct and adjoint equations

To linearize the Navier-Stokes (NS) equations, the fluid variables are decomposed into a steady and a disturbance field: $\boldsymbol{u} = U_b + \boldsymbol{u}'$ and $p = p_b + p'$. (U_b, p_b) are the nonlinear steady flow variables and they are obtained by omitting the unsteady terms in Eq. (2) with a Newton method. $(\boldsymbol{u}', p')$ are the perturbation fields of the fluid velocity and pressure, respectively.

The displacement, velocity, and acceleration of the cylinder can be decomposed as

$$\eta = \eta_s + \eta', \quad \zeta = \zeta_s + \zeta', \quad \xi = \xi_s + \xi', \tag{12}$$

where the subscript s denotes the steady state; η', ζ', and ξ' represent the disturbance variables of the cylinder's displacement, velocity, and acceleration, respectively. At the steady state, the cylinder remains stationary at the origin with zero acceleration, and hence $\eta_s = \zeta_s = \xi_s = 0$.

By substituting the decomposed flow and structural variables into Eqs. (1)–(5), and subsequently subtracting the steady-state equations, the equations governing the evolution of the disturbance field can be derived. We assume the disturbances are small and thus neglect the nonlinear terms. This leads to the following linearized equations of the disturbance field:

$$\boldsymbol{\nabla}\cdot\boldsymbol{u}' = 0, \tag{13}$$

$$\frac{\partial\boldsymbol{u}'}{\partial t} + (\boldsymbol{u}'\cdot\boldsymbol{\nabla})U_b + (U_b\cdot\boldsymbol{\nabla})\boldsymbol{u}' + \boldsymbol{\nabla}p' - \frac{1}{\text{Re}}\nabla^2\boldsymbol{u}' - (\zeta'\boldsymbol{n}_y\cdot\boldsymbol{\nabla})U_b = 0, \tag{14}$$

$$\frac{\partial\eta'}{\partial t} - \zeta' = 0, \tag{15}$$

$$\frac{\partial\zeta'}{\partial t} - \xi' = 0, \tag{16}$$

$$\xi' + \frac{4\pi\gamma}{U^*}\zeta' + \left(\frac{2\pi}{U^*}\right)^2\eta - \frac{4}{\pi m}[\boldsymbol{F}_p(p') + \boldsymbol{F}_u(\boldsymbol{u}')] = 0. \tag{17}$$

The linearized system has the same boundary conditions as the NS equations except for the inlet, upper, and lower boundaries at which a Dirichlet condition $\boldsymbol{u}' = 0$ is applied.

Next, we derive the linearized adjoint equations. For any linear operator L', the adjoint operator $L^{\dagger}$ is defined such that it satisfies the Lagrange identity

$$\langle L^{\dagger} p, q \rangle = \langle p, L'q \rangle \tag{18}$$

for any arbitrary vectors q and p in the domain of L' and $L^{\dagger}$, respectively. The notation $\langle \cdot, \cdot \rangle$ denotes the inner product under which the above identity holds. In the current context of VIV, the direct operator L' represents the linearized Navier-Stokes equations (13)–(17). $L^{\dagger}$ is the corresponding adjoint operator with the definition of the inner product as the integral over the domain Ω and the time horizon T_0:

$$\langle p, q \rangle = \int_{T_0} \int_{\Omega} p^T q \, d\Omega dt. \tag{19}$$

We define the vector $q' = (u', p', \eta', \zeta', \xi')^T$, which lies in the domain of L, and an adjoint vector $q^{\dagger} = (u^{\dagger}, p^{\dagger}, \eta^{\dagger}, \zeta^{\dagger}, \xi^{\dagger})^T$, which lies in the domain of $L^{\dagger}$. The adjoint equations can be obtained by taking the inner product between the adjoint variables and the direct equations. The use of integration by parts, the divergence theorem, and a judicious manipulation of terms leads to a set of expressions for the adjoint equations. The full derivation of the equations along with the boundary conditions can be found in Appendix A. The final set of adjoint equations for FSI of a 2D oscillating cylinder is expressed as

$$\nabla \cdot u^{\dagger} - \frac{4}{\pi m} F_p \xi^{\dagger} = 0, \tag{20}$$

$$-\frac{\partial u^{\dagger}}{\partial t} - \nabla u^{\dagger} \cdot U_b + (\nabla U_b)^T \cdot u^{\dagger} + \nabla p^{\dagger} - \frac{1}{\text{Re}} \nabla^2 u^{\dagger} - \frac{4}{\pi m} F_u \xi^{\dagger} = 0, \tag{21}$$

$$-\frac{\partial \eta^{\dagger}}{\partial t} + \left(\frac{2\pi}{U^*}\right)^2 \xi^{\dagger} = 0, \tag{22}$$

$$-\frac{\partial \zeta^{\dagger}}{\partial t} - n_y \cdot (\nabla U_b)^T \cdot u^{\dagger} - \eta^{\dagger} + \frac{4\pi \gamma}{U^*} \xi^{\dagger} = 0, \tag{23}$$

$$\xi^{\dagger} - \zeta^{\dagger} = 0. \tag{24}$$

The adjoint equations evolve the adjoint field backward in time, and it is possible to reintroduce forward propagation by employing a variable substitution of $\tau = -t$. Moreover, we also conduct global LSA of this coupled fluid-structure system. Direct and adjoint perturbation variables can be expressed in the form of an eigenmode:

$$q' = \hat{q}' e^{i\omega t}, \quad q^{\dagger} = \hat{q}^{\dagger} e^{i\omega^{\dagger} t}, \tag{25}$$

where ω is the eigenvalue and is generally expected to be a complex number ($\omega = \omega_r + i\omega_i$); $\omega^{\dagger}$ is the adjoint eigenvalue. The imaginary part ω_i corresponds to the amplification rate, and the real part ω_r is the angular frequency. $\hat{q}'$ and $\hat{q}^{\dagger}$ are the shape functions. The following eigenvalue problem for global linear instability is obtained,

$$\omega N\hat{q}' = M'\hat{q}', \quad \omega^{\dagger} N\hat{q}^{\dagger} = M^{\dagger}\hat{q}^{\dagger}, \tag{26}$$

where the matrix form of the direct operator can now be written as follows:

$$M' = \begin{bmatrix} M_f & -\nabla & 0 & (n_y \cdot \nabla)U_b & 0 \\ \nabla \cdot & 0 & 0 & 0 & 0 \\ 0 & 0 & 0 & 1 & 0 \\ 0 & 0 & 0 & 0 & 1 \\ 4F_u/\pi m & 4F_p/\pi m & -(2\pi/U^*)^2 & -4\pi \gamma/U^* & -1 \end{bmatrix}, \tag{27}$$

where 'O' represents the matrix, '$\mathbf{0}$' is the row/column vector, and the mass matrix N is given by

$$N = \begin{bmatrix} I & 0 & 0 & 0 & 0 \\ 0 & 0 & 0 & 0 & 0 \\ 0 & 0 & 1 & 0 & 0 \\ 0 & 0 & 0 & 1 & 0 \\ 0 & 0 & 0 & 0 & 0 \end{bmatrix}. \tag{28}$$

Also, we can define the adjoint operator in matrix form as

$$M^{\dagger} = \begin{bmatrix} M_f^{\dagger} & -\nabla & 0 & 0 & 4F_u/\pi m \\ -\nabla\cdot & 0 & 0 & 0 & 4F_p/\pi m \\ 0 & 0 & 0 & 0 & -(2\pi/U^*)^2 \\ n_y \cdot (\nabla U_b)^T\cdot & 0 & 1 & 0 & -4\pi\gamma/U^* \\ 0 & 0 & 0 & 1 & -1 \end{bmatrix}, \tag{29}$$

where M_f and $M_f^{\dagger}$ are the fluid operators, defined as

$$M_f = -U_b \cdot \nabla - \nabla U_b \cdot + \mathrm{Re}^{-1}\nabla^2,$$
$$M_f^{\dagger} = U_b \cdot \nabla - (\nabla U_b)^T \cdot + \mathrm{Re}^{-1}\nabla^2. \tag{30}$$

After discretization, the operator $M^{\dagger}$ is the conjugate transpose of M' [50,53]. Here, we define (*) as the complex conjugate transpose of the matrix.

C. BPOD ROM for unstable VIV flows

The development of a BPOD ROM is based on continuous-time, linear direct, and adjoint state-space systems:

$$N\frac{d\boldsymbol{q}'}{dt} = M'\boldsymbol{q}' + Bu, \quad y = C\boldsymbol{q}',$$
$$N\frac{d\boldsymbol{q}^{\dagger}}{dt} = M^*\boldsymbol{q}^{\dagger} + C^*v, \quad w = B^*\boldsymbol{q}^{\dagger}, \tag{31}$$

where M^* is the discrete adjoint operator; B and C are the time-independent input and output matrices for the direct state, respectively, while C^* and B^* are those for adjoint state; and (u, y) and (v, w) are the corresponding direct and adjoint input and output variables.

Moore [54] and Rowley [20] introduced a snapshot-based approximate BPOD method, in which snapshots are collected from the impulse response of the above direct and adjoint systems in Eqs. (31) as follows:

$$\boldsymbol{P} = [\boldsymbol{q}'(t_1), \boldsymbol{q}'(t_2), \ldots, \boldsymbol{q}'(t_m)],$$
$$\boldsymbol{Q} = [\boldsymbol{q}^{\dagger}(t_1), \boldsymbol{q}^{\dagger}(t_2), \ldots, \boldsymbol{q}^{\dagger}(t_m)]. \tag{32}$$

Then, these two series of snapshots are used to construct approximate controllability and observability Gramians [55] as

$$G_c = \int_0^{\infty} e^{M't} BB^* e^{M^*t} dt \approx \sum_{i=1}^{N} \boldsymbol{q}'(i\Delta t)[\boldsymbol{q}'(i\Delta t)]^* \delta_i = PP^*,$$

$$G_o = \int_0^{\infty} e^{M^*t} C^*C e^{M't} dt \approx \sum_{i=1}^{N} \boldsymbol{q}^{\dagger}(i\Delta t)[\boldsymbol{q}^{\dagger}(i\Delta t)]^* \delta_i = QQ^*, \tag{33}$$
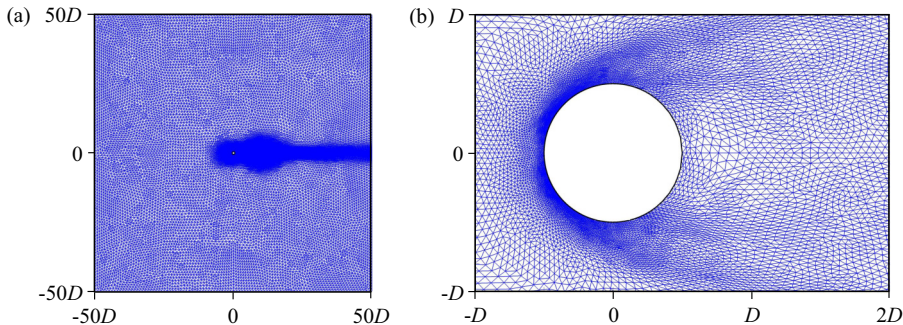
FIG. 2. (a) Overview of the computational mesh and (b) enlarged view near the cylinder.

where δ_i refers to quadrature coefficients and Δt denotes the time-step size. The balancing transformation $\boldsymbol{\Phi}$ and its inverse transform $\boldsymbol{\Psi}$ can be simply given as

$$\boldsymbol{\Phi} = \boldsymbol{P}\boldsymbol{V}\boldsymbol{\Sigma}^{-1/2}, \quad \boldsymbol{\Psi} = \boldsymbol{Q}\boldsymbol{U}\boldsymbol{\Sigma}^{-1/2}, \tag{34}$$

where $\boldsymbol{U}$, $\boldsymbol{\Sigma}$, and $\boldsymbol{V}$ are determined from the singular value decompositions (SVDs) of the cross-Gramian $\boldsymbol{Q}^*\boldsymbol{P}$ given by

$$\boldsymbol{Q}^*\boldsymbol{P} = \boldsymbol{U}\boldsymbol{\Sigma}\boldsymbol{V}^* = [\boldsymbol{U}_1 \quad \boldsymbol{U}_2]\begin{bmatrix}\boldsymbol{\Sigma}_1 & 0 \\ 0 & \boldsymbol{\Sigma}_2\end{bmatrix}\begin{bmatrix}\boldsymbol{V}_1^* \\ \boldsymbol{V}_2^*\end{bmatrix}. \tag{35}$$

The columns of $\boldsymbol{\Phi}$ are the balanced direct modes and the columns of $\boldsymbol{\Psi}$ are the balanced adjoint modes. $\boldsymbol{\Sigma} = \mathrm{diag}([h_1 \cdots h_n])$ with $h_1 \geqslant h_2 \geqslant \cdots \geqslant h_n$ are the Hankel singular values (HSVs) of the system. HSVs provide an indication of system's dynamical significance, which ranks the balanced system according to its joint controllability and observability. Flinois *et al.* have proved that the BPOD method can be directly applied to an unstable system [16]. Therefore, we employ this projection-free method to construct the BPOD ROM for unstable VIV.

III. NUMERICAL METHODS AND VALIDATIONS

Both direct numerical simulation and global linear instability analysis are performed using the open-source finite element method solver FREEFEM++ [56]. All equations are first reformulated into a variational form (elaborated in Ref. [38]), then discretized spatially using the Delaunay-Voronoi algorithm, and managed through the MUMPS library for direct lower-and upper (LU) inversion. For spatial discretization, the velocity field is discretized using quadratic (P_2) elements, while the spatial discretization of the pressure field is achieved by using the Taylor-Hood basis (P_1) elements. An unstructured triangular mesh is used, as shown in Fig. 2. For time discretization, a second-order backward difference is employed. The time-step size Δt is determined based on the Courant-Friedrichs-Lewy conditions, with a Courant number set to 0.1.

Verification of the numerical methods, together with mesh independence assessment, are carried out by solving the generalized eigenvalue problem of the linear direct problem [Eq. (26)] using a shift-and-invert Arnoldi method from the ARPACK library [57]. The leading eigenvalues obtained using different meshes are shown in Table I. The results obtained with M_2 and M_3 have shown good agreement with the results from Sabino *et al.* [38]. For ease of computation, we use the M_2 mesh for the numerical simulations within this work.

Moreover, validation of the adjoint equation can be achieved by comparing the eigenspectrum of the direct and adjoint problems [28]. The eigenvalues of the adjoint problem are the complex conjugates of those of the direct problem. For real matrices, the eigenspectra for both problems should exhibit the same distribution. As depicted in Fig. 3, for problems with Re = 60 and

TABLE I. Resolution parameters of meshes and the results. M_i is the total number of unstructured triangle mesh. ω_i and ω_r are eigenvalues at Re $= 60$ with $(m, U^*) = (20, 8)$.

Mesh	$M_1(14340)$	$M_2(57360)$	$M_3(229440)$	Ref. [38]
ω_i	0.0781	0.0747	0.0732	0.0735
ω_r	0.758	0.761	0.760	0.760

$(m, U^*) = (20, 8)$, a good agreement between the direct and adjoint eigenspectra is observed, confirming the correct derivation of the linear adjoint equations.

IV. RESULTS AND DISCUSSION

In this section, we begin by conducting the global linear instability analysis of the VIV system. The primary objective is to provide insights into the control mechanism that are discussed subsequently. We then construct the BPOD ROM for the unstable VIV flow. Following this, we discuss the selection of control parameters and the placement of actuators and probes. Finally, we proceed to develop a control strategy on the BPOD-based ROM and successfully apply it to the control of the FOM.

A. Global linear instability analysis of FOM

We first perform a global linear instability analysis of the coupled full-order VIV problem. Specifically, we analyze the eigenvalue characteristics for two mass ratios ($m = 20$ and 5) and reduced velocities within the range $U^* \in (0, 100)$, under different Reynolds numbers Re $= 60$, 80, and 100. For $m = 20$, we observe two distinct branches of unstable eigenmodes, which are represented by open and solid markers in Fig. 4(a). These two branches of eigenmodes are known as the fluid mode (FM) and the elastic mode (EM) [58,59]. Their distributions show similarity across three tested Reynolds numbers. As U^* varies, these two modes remain uncoupled, and the FM consistently emerges as the primary unstable mode in VIV flow, forming a closed ring that rotates clockwise with increasing U^*. The end points ($U^* \rightarrow \infty$) of the FM approach the stationary wake modes (denoted as origin dots P, Q, and R). Additionally, as the Reynolds number increases, there is a corresponding decrease in the area of the ring, leading it to converge towards the stationary wake modes. This observation suggests that, under high Reynolds numbers, the growth rate and frequency for the FM nearly remain constant. For $m = 5$, the two leading eigenmodes do not exhibit a distinct characteristic, whether it be as elastic mode or fluid mode. Instead, they appear as an interconnected curve as shown in Fig. 4(b). We identify these two interconnected modes as fluid-elastic mode I
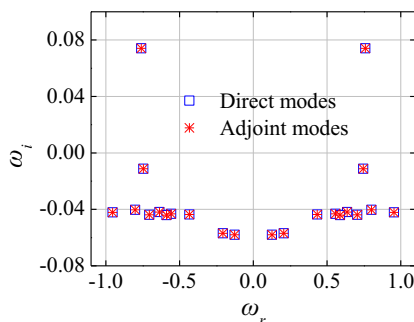

FIG. 3. Comparison of the eigenspectrum for direct and adjoint modes: real and imaginary parts of eigenvalues at Re $= 60$ with $(m, U^*) = (20, 8)$.
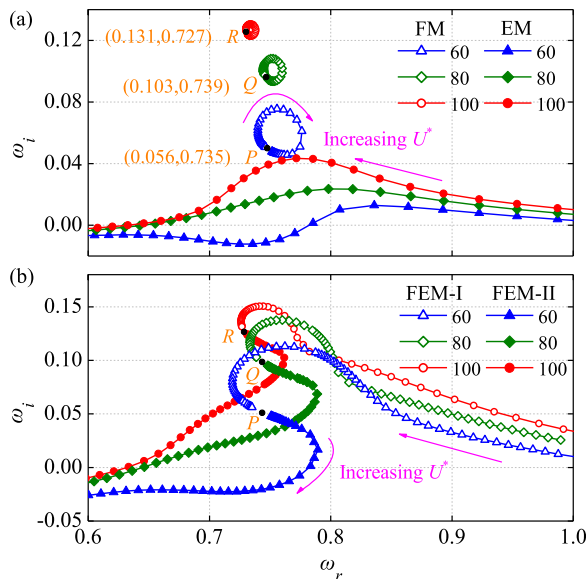
FIG. 4. The change of eigenvalues across $U^* \in (0, 100)$ for (a) $m = 20$ and (b) $m = 5$, at Reynolds numbers Re = 60, 80, and 100 (represented by blue, green, and red, respectively). Black dots P, Q, and R correspond to eigenvalues of stationary cylinder cases.

(FEM-I) and fluid-elastic mode II (FEM-II). At low U^*, FEM-I exhibits resemblances to the elastic mode, similar to the characteristics of the EM for $m = 20$. As $U^* \to \infty$, FEM-I approaches to the point corresponding to the stationary wake mode. In contrast, FEM-II originates from the stationary mode at small U^* value. Further insight into the influence of Reynolds number and mass ratio on coupled and uncoupled eigenvalues can be found in Ref. [58].

Here, we choose Re = 80 as the representative case and further study its behavior for the leading eigenmodes. Note that all results and discussions in the following sections are focused on this Reynolds number, except for specific cases. Figure 5(a) shows the variation in the growth rate of FM and EM across $U^* \in [3.0, 12.0]$ for $m = 20$. The FM appears as the leading mode and remains constantly unstable. The EM becomes unstable within $U^* \in [5.8, 9.3]$. The FM and EM achieve
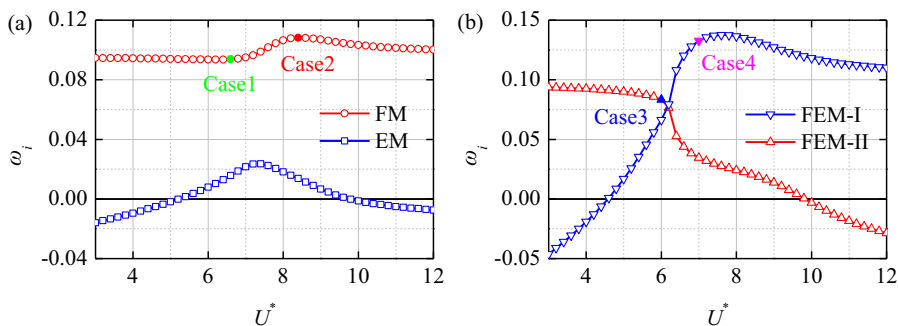

FIG. 5. The change of linear increase rate ω_i with reduced speed U^* for (a) $m = 20$ and (b) $m = 5$. We use these four cases to discuss the structure sensitivity in Sec. IV C. These four cases are selected such that they have relatively large differences in spatial distribution of structure sensitivity throughout the range of $U^* \in (0, 100)$.
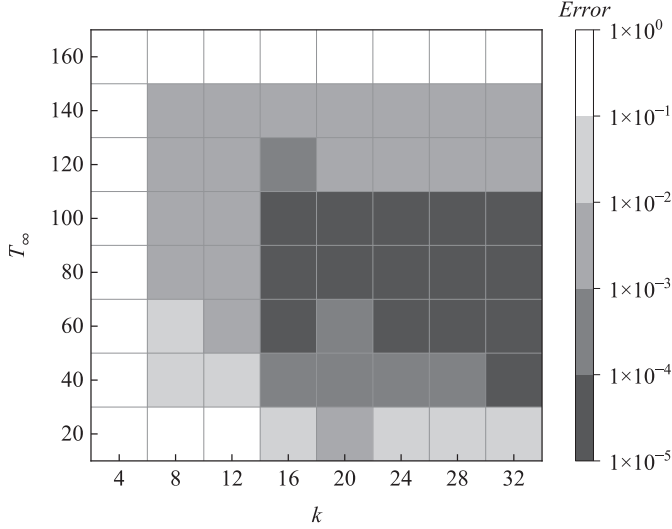
FIG. 6. Error of the ROM varies with the change of final simulation time T_∞ and ROM rank k.

their maximum growth rates at $U^* = 8.4$ and 7.4, respectively. Figure 5(b) shows the variation in the growth rate of FEM-I and FEM-II with U^* for $m = 5.0$. As U^* increases, FEM-II initially becomes the leading unstable mode (when $U^* < 6.2$), after which it is succeeded by FEM-I. These behaviors of modes offer valuable insights into interpreting the controlled flow dynamics, as elaborated in the following section.

B. BPOD modeling of VIV

In this study, we use a projection-free method for BPOD modeling [16]. This method needs to select a suitable final simulation time T_∞, because only the leading unstable mode can be retained and the initial transition information from the impulse response will be lost for excessively large final simulation time. During BPOD modeling, snapshots are collected from $t = 0$ to T_∞ with intervals of $10\Delta t$ for both direct and adjoint simulations in which a constant time step of $\Delta t = 0.01$ is used. To validate our methodology, we define a transfer function of the plant as

$$T_P(s) = \boldsymbol{C}(s\boldsymbol{I} - \boldsymbol{M})^{-1}\boldsymbol{B}, \tag{36}$$

where s is the angular frequency. The error between the FOM and ROM is defined as

$$\text{error} = \left[\frac{\int_{-\infty}^{+\infty} |T_P - \bar{T}_P|^2 ds}{\int_{-\infty}^{+\infty} |T_P|^2 ds} \right]^{\frac{1}{2}}. \tag{37}$$

The final simulation time T_∞ and ROM rank k are two parameters that decide the accuracy of the ROM. We select a case of Re $= 80$ and $(m, U^*) = (20, 12)$ as an illustration. Figure 6 shows that the error of the ROM varies with the change of final simulation time T_∞ and ROM rank k. In this work, we construct BPOD models with $k = 20$ and $T_\infty = 50$, which keeps the error to less than 0.001. It is clear that the ROM successfully reproduces the impulse response of the FOM during the initial transitions shown in Fig. 7(a) and over time spans surpassing the final simulation time used in Fig. 7(b). Moreover, a good match of transfer function in Fig. 7(c) also demonstrates that the BPOD ROM has remarkable accuracy.

We display the Hankel singular values in Fig. 7(d), which provides insight into the controllability and observability of the associated balanced modes. Figure 8 shows the spatial pattern of the direct and adjoint BPOD modes corresponding to the first and second singular values. When comparing the
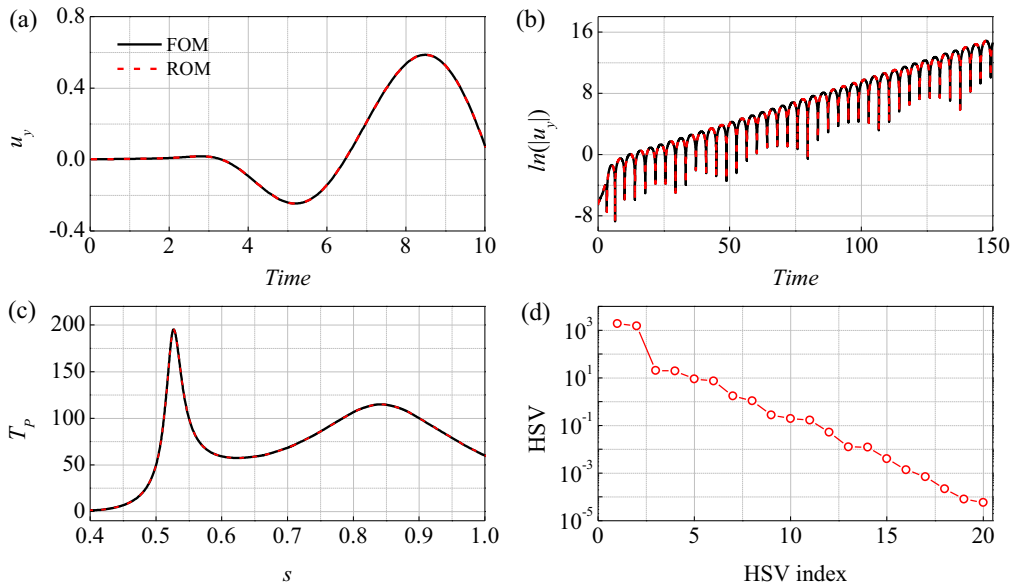
FIG. 7. [(a) and (b)] A comparison of the impulse response between the FOM and the 20th-order ROM. (c) Transfer function T_P obtained from the ROM compared with that of the FOM. (d) The first 20 Hankel singular value distributions.

first and second modes, similar structures can be observed. For both modes, the associated direct modes [Figs. 8(a) and 8(c)] encompass the probe locations, while the adjoint modes [Figs. 8(b) and 8(d)] exhibit pronounced amplitudes in proximity to the actuators. The latter characteristic significantly enhances controllability.

C. Control parameter selection and actuator and probe placement

We design the feedback controller based on the LQG framework as detailed in Appendix B. The noise covariance ratio (R) and the control cost (G) are two control parameters that influence the effectiveness of the LQG controller. In this section, we conduct a quantitative analysis of the stability margins of the LQG controller within the closed-loop system, which informs our control
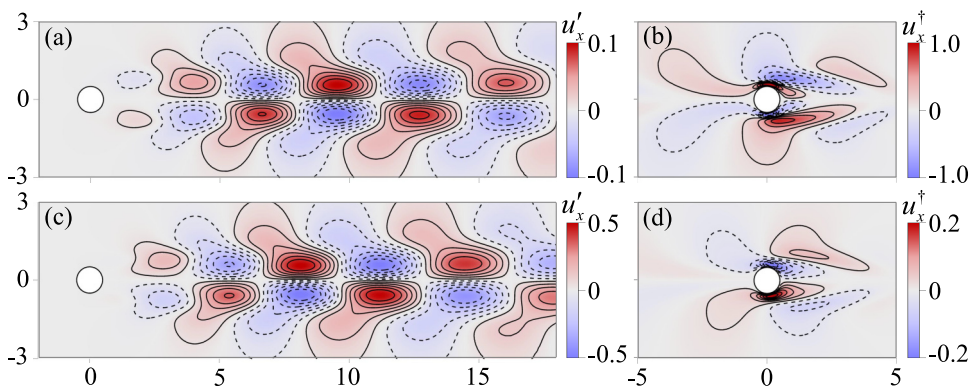

FIG. 8. The (a) first and (c) second direct BPOD modes visualized through the contours of the streamwise velocity component; [(b) and (d)] the corresponding adjoint BPOD modes.
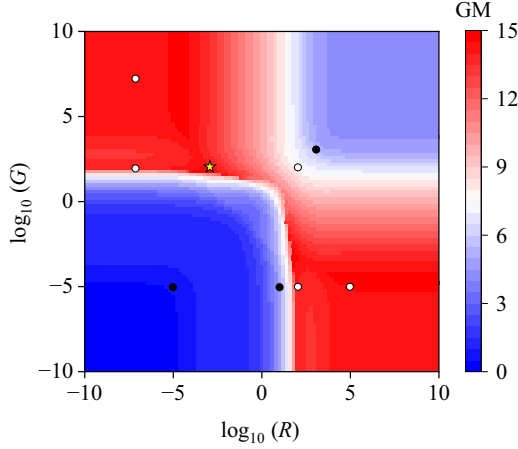
FIG. 9. Contours of gain margin (GM) plotted in the $\log_{10}(R) - \log_{10}(G)$ plane for VIV at Re = 80, with $(m, U^*) = (20, 12)$. After testing in the control FOM, the black symbols indicate stable compensated numerical simulations, while white symbols mark unstable compensated simulations. The yellow star with $(R, G) = (10^{-3}, 10^2)$ represents the selected control parameter in this work.

parameter selection criteria and guides optimal placement strategy for actuators and probes. To calculate the stability margins, two types of perturbations are applied: (i) a change in the magnitude of the transfer function and (ii) a change in the phase of the transfer function. We have

$$\bar{T}_p \longrightarrow a\bar{T}_P, \quad \bar{T}_P \longrightarrow e^{i\phi}\bar{T}_P, \tag{38}$$

where the first modification represents an error in the growth rates; the second modification represents an error in the travel time of perturbations between the actuators and probes.

Stability margins are quantified by GM and phase margin (PM) here. The GM is expressed in decibels (dB) with a definition of GM $= 20\log_{10} a^+ - 20\log_{10} a^-$, where $a^+ > 1$ is the minimum value of the amplitude a that achieves marginal stability in the transfer function $w \to n$. That is, we need to seek a to ensure that $1 - a\bar{T}_P\bar{T}_K$ has one zero with zero real part while all other zeros are located in the left half-plane. The maximum gain margin $a^- < 1$ has a similar definition of a^+, corresponding to the maximum value of amplitude a that achieves marginal stability. The phase margin is the minimum positive value of ϕ such that $1 - e^{i\phi}\bar{T}_P\bar{T}_K$ exhibits a marginal zero.

We define the amplitude function $f(a)$ and phase angle function $g(\phi)$ as [60]

$$f(a) = \max\{1 - a\bar{T}_P(s)\bar{T}_K(s) = 0\},$$
$$g(\phi) = \max\{1 - e^{i\phi}\bar{T}_P(s)\bar{T}_K(s) = 0\}, \tag{39}$$

where $\bar{T}_K$ is the transfer function of the compensated system, as

$$\bar{T}_K(s) = \boldsymbol{K}(s\boldsymbol{I} - \boldsymbol{J})^{-1}\boldsymbol{L}, \tag{40}$$

a^+ is the smallest zero of f greater than one, while a^- is the largest zero of f less than one. The PM is the smallest positive zero of g.

Figure 9 displays the GM as a function of the noise covariance ratio (R) and the control cost (G) for a compensator designed at Re = 80 with $(m, U^*) = (20, 12)$. The stability margin directly influences the effectiveness of the LQG controller. White circles added in the (R, G) plane indicate that VIV of the full-order model can be suppressed through testing. Black circles indicate that the controller loses its effect, with GM less than 6 and phase margin less than 18. Therefore, the selection of LQG control parameters (R, G) should located in a red region with a high stability
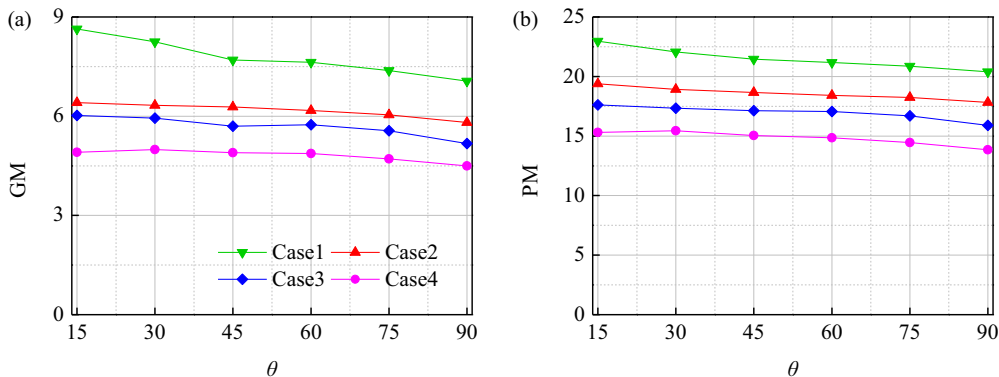
FIG. 10. (a) GM and (b) PM at different actuator angles θ while maintaining the same probe positions at $(x, y) = (3.0, \pm 0.5)$ for Cases1–4.

margin. In this study, we select a constant control parameter: $(R, G) = (10^{-3}, 10^2)$ marked by a yellow star with GM = 14.5 and PM = 42.1.

BPOD modes can only give a general view for actuator and probe placement. To enhance the performance of feedback flow control, we seek to optimize the placement of probes and actuators. We first study the influence of actuator placement on stability margins while keeping the probes fixed at position $(x, y) = (3.0, \pm 0.5)$. We conduct four groups of tests, aligned with the parameters of cases 1–4. In each group, the actuator positions vary from $\theta = 15°$ to $90°$, with an interval of $\Delta\theta = 15°$. Figure 10 shows values of GM and PM at different actuator positions θ. We find that the change of PM has the same trend as that of GM, i.e., a large GM corresponding to a large PM. It can be seen that stability margins increase as the angles increase for all four cases. However, the relative error difference, defined as $\Delta\text{GM} = (\text{GM}_{15°} - \text{GM}_{90°})/\text{GM}_{15°}$, remains below 15% for all cases. Therefore, we can neglect the influence of the actuator's distribution on control robustness. The decrease in GM along θ can be attributed to the increased distance between the input and output, leading to greater control delay, which is analogous to the effect of a larger value of x for probes.

Optimal probe locations are selected by comparing the widely adopted wavemaker regions and the spatial distribution of averaged controller gain margin. The former is calculated by overlapping the leading direct and adjoint eigenmodes, following the method outlined by Negi *et al.* [28]:

$$\mathbf{\Theta}(x, y) = \frac{|\hat{\boldsymbol{q}}'(x, y)||\hat{\boldsymbol{q}}^\dagger(x, y)|}{\langle \hat{\boldsymbol{q}}'(x, y), \hat{\boldsymbol{q}}^\dagger(x, y) \rangle}, \quad (41)$$

where $\mathbf{\Theta}(x, y)$ provides an indication of the region where localized feedback will produce a large shift in the eigenvalue, thus representing the sensitivity of the eigenvalue to structural perturbations.

Figures 11(a) and 11(b) illustrate the structural sensitivity regions for four distinct cases. Specifically, Case1 and Case2 are two representative cases with $m = 20$, featuring reduced speeds of $U^* = 6.6$ and $U^* = 8.4$, respectively, within the FM branch. Notably, Case1 exhibits the highest increase rate, while Case2 demonstrates the lowest increase rate among all U^* values depicted as the green circle in Fig. 4(a). Hence, their structural sensitivity regions [Fig. 11(a)] display the most significant spatial difference. On the other hand, cases 3 and 4 are two representative cases with $m = 5$, featuring reduced speeds of $U^* = 6.0$ and $U^* = 7.0$, respectively, within the FEM-I branch. It is evident that the peak of the wavemaker region for Case1 is located farther from the cylinder (at $x = 3.2$), while for Case2, it is closer to the cylinder at $x = 2.4$, compared to the stationary cylinder case ($x = 3.0$, not shown here). Different from cases 1 and 2, Case3 is sensitive to structural perturbations not only in the near-wake region ($x < 1.0$) but also in the far-wake region ($x = 3.8$). Notably, Case4 differs from the other three cases, as its high-sensitivity region is located in the small near-wake region that surrounds the cylinder, while the far-wake wavemaker region becomes less
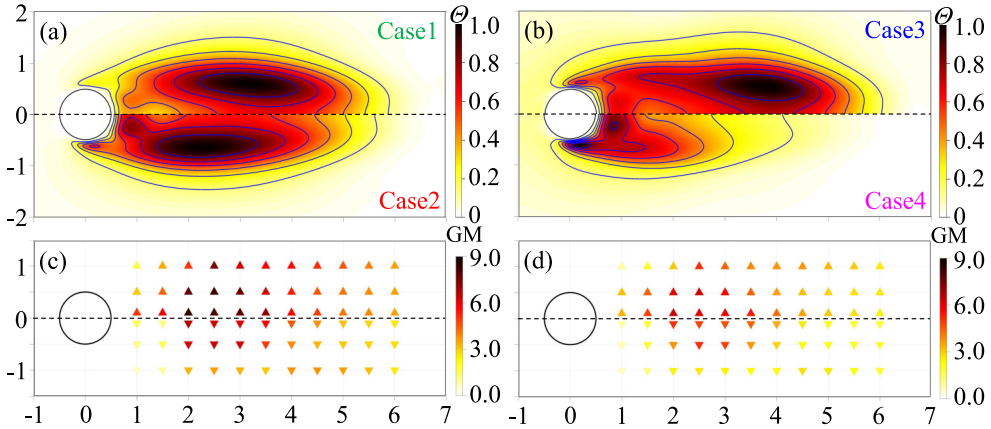
FIG. 11. Structural sensitivity region for (a) $m = 20$ and (b) $m = 5$,with different reduced speeds. Cases 1–4 are the cases illustrated in Fig. 5. The regions are symmetrically positioned with respect to the horizontal axis, so only half is plotted. [(c) and (d)] Robustness study with the same actuator position ($\theta = 45°$) but different placement of probes.

prominent. For all cases, the distribution of high-sensitivity regions along the y axis is concentrated near $y = \pm 0.5$. As U^* increases significantly, the sensitivity map begins to resemble the stationary case. More studies about the structural sensitivity of VIV flow can be found in Ref. [28].

We then examine the individual effects of actuator and probe locations on control gain margin. First, we study the influence of probes on the control robustness while maintaining the actuator positions fixed at $\theta = 45°$. Four groups of tests are carried out, in which the parameters (mass ratios and reduced speeds) align with those used in Cases1–4 above. The LQG controller applies the same control parameter $(R, G) = (10^{-3}, 10^2)$ across all four test cases. Figures 11(c) and 11(d) illustrate the averaged gain margin at 33 positions for each case, within a spatial range $(x, y) \in (1.0, 6.0) \times (\pm 0.1, \pm 1.0)$ for Cases1–4. From this analysis, we can derive three key conclusions:

(i) High-gain-margin regions exhibit weak dependence on mass ratio and reduced speed. Despite notable variations in wavemaker regions, there is a consistent spatial distribution pattern evident in the high-robustness maps across all four cases.

(ii) The averaged gain margin demonstrates a decreasing trend from Case1 to Case4, and thus a decreasing trend of controllability. This implies that the systems with higher mass ratios are easier to control compared to those with lower mass ratios.

(iii) A consistently observed pattern across all cases is the existence of a high-robustness region near $x = 3.0$. In regions both too close to and too far from the cylinder, robustness tends to diminish. This points to a fundamental trade-off where the probe should be positioned close enough to the cylinder to minimize time delays caused by convection, while simultaneously being positioned sufficiently far from the cylinder to capture crucial information (e.g., unstable eigenmodes) as they develop downstream. Similar findings have been reported in the work of Jin et al. [11], where they utilized a resolvent-based modeling approach to suppress vortex shedding in stationary cylinder flow.

Next, we study the influence of Reynolds number on stability margins. Figure 12 presents the change in control gain margin as Reynolds numbers vary from Re = 60 to 120, considering different probe positions at $y = \pm 0.5$ and $(m, U^*) = (20, 12)$. Both actuator position ($\theta = 45°$) and LQG controller parameters $(R, G) = (10^{-3}, 10^2)$ remain consistent. It is evident that the control gain margin decreases as Reynolds numbers increase. Controllability also diminishes. Our numerical experiments show that the controller can effectively control VIV with a Reynolds number of up to
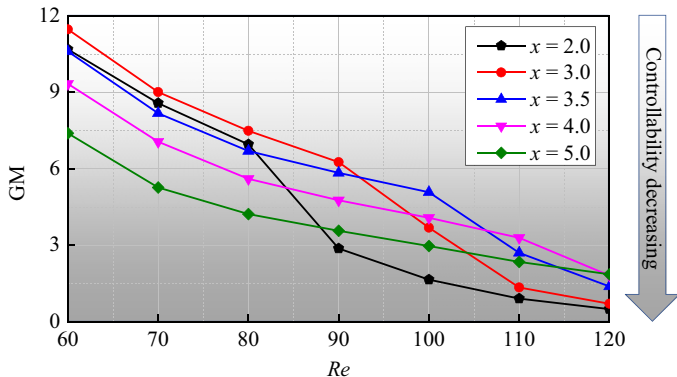
FIG. 12. Control gain margin variation across Reynolds numbers for different probe positions, while keeping the actuator position fixed at $\theta = 45°$, with $(m, U^*) = (20, 12)$. The controllability of the FOM decreases with the decreasing of GM.

Re = 100, beyond which we are unable to suppress the amplification of unstable modes. Moreover, the controller cannot suppress VIV when GM < 6 and PM < 18.

The optimal sensor location with the highest GM shifts from $x = 3.0$ (for Re < 90) to $x = 3.5$ (for Re = 100) and further to $x = 4.0$ (Re = 110 and 120). The aforementioned trade-off becomes progressively challenging to maintain with increasing Reynolds numbers, resulting in a linear downstream shift of the optimal sensor location. Overall, given controllability constraints, positioning probes close to $x = 3.0$ emerges as an ideal strategy within our control approach.

D. Closed-loop control of VIV based on BPOD ROM

Next, we control the full-order model. Control parameters are determined by the LQG with the BPOD ROM and these parameters are then tested in the FOM model. Our objective is to establish a control strategy capable of effectively controlling VIV flows, which can also suit a range of Reynolds number. For each of these cases, a consistent control strategy is implemented, involving (i) the actuator position at $\theta = 45°$, (ii) a pair of sensors located at $(x, y) = (3.0, \pm0.5)$, and (iii) LQG parameters $(R, G) = (10^{-3}, 10^2)$. Figure 13 illustrates the leading eigenvalues of both the BPOD ROM matrix $\bar{M}'$ and those of the LQG compensated system matrix J (i.e., after control) for four cases, facilitating a comparison of the system's attributes before and after control. The circles represent the state before control, demonstrating that the BPOD ROM effectively reconstructs all unstable eigenvalues alongside the dominant stable eigenvalues. The plus sign signifies the postcontrol state, demonstrating that the LQG controller effectively controls VIV in all four cases. It is noteworthy that the leading eigenvalue after control (green plus signs) predicts the long-term behavior of the controlled flow. In other words, the perturbation of the controlled flow is expected to decay in time with a rate of ω_i together with an oscillation angular frequency ω_r after a long duration. We have observed that the control effectively changes the eigenmodes of the system. Specifically, for $m = 20$, the elastic modes have changed to steady modes [the two green plus sign in Figs. 13(a) and 13(b)]. For $m = 5$, a new mode [the two green plus signs in Figs. 13(c) and 13(d)] is created.

We then apply the above LQG controller to control the full-order model. In the DNS for the FOM, the VIV is triggered by introducing an initial perturbation associated with the leading mode with a magnitude of 10^{-5}. Figure 14(a) illustrates the temporal evolution of the velocity at the probe location for the case with $(m, U^*) = (20, 12)$. It can be clearly seen that the VIV progresses through two distinct phases, as illustrated by the black line. The first phase is characterized by linear amplification (when $t < 60$), with a growth rate of $k = 0.0991$. The second phase represents saturation oscillation, occurring when $t > 100$. In this study, we aim at controlling the VIV during
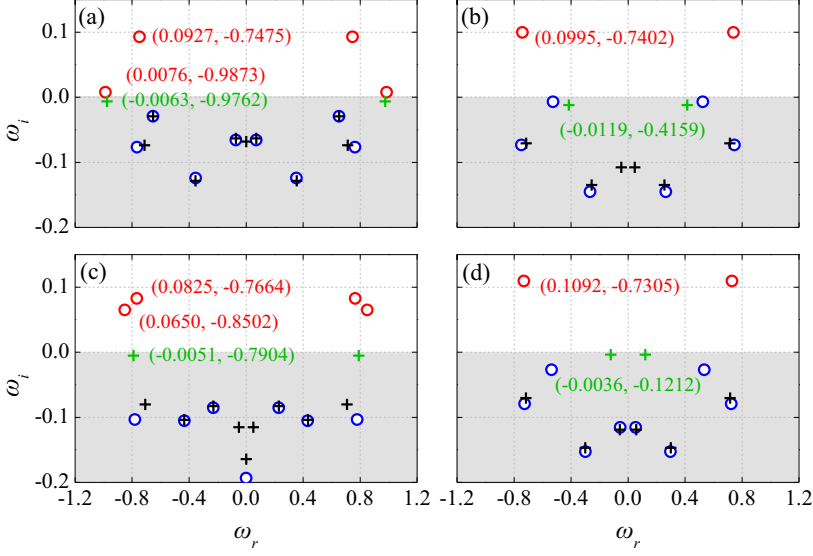
FIG. 13. Eigenvalue spectrum for the ROM with and without control for (a) $(m, U^*) = (20, 6)$, (b) $(m, U^*) = (20, 12)$, (c) $(m, U^*) = (5, 6)$, and (d) $(m, U^*) = (5, 12)$. The grey shaded region represents the stable state. Red and blue circles denote unstable and stable modes without control, respectively. The plus signs denote the modes with control, where the green plus signs decide the long-term behavior of the VIV system.

its early stages, and hence we initiate control during the VIV's linear phase at $t = 50$. It is worth noting that the control strategy is robust against variations in the starting time, and such variations do not affect the asymptotic behavior. The flow's response with control at the probe is illustrated by the red line in Fig. 14(a), which can be divided into three phases, namely, the phase of instantaneous growth ($50 < t < 60$), the subsequent phase of multimode decay ($60 < t < 150$), and, finally, the asymptotic decay phase ($t > 150$). As shown in Fig. 14(d), during the phase of instantaneous growth, a large and abrupt control action occurs. This strong control action introduces extra perturbation energy into the system and reshapes the mean flow structures, consequently stimulating an amplification of nonmodal energy. This amplification is evident in Figs. 14(b) and 14(c), where larger values of u_y and cylinder amplitude η are observed, as compared to those at $t = 50$. Here, we use the snapshot-based proper orthogonal decomposition (POD) method to analyze this transition growth [61]. The spatiotemporal vorticity field can be decomposed as

$$\chi(x, t) = \sum_{i=1}^{N} a_i(t)\phi_i(x), \tag{42}$$

where N represents the number of snapshots used in the calculation. The SVD is applied to calculate the spatial mode $\phi_i(x)$ and their corresponding temporal mode $a_i(t)$, given by

$$(\phi, \sigma, a) = \text{SVD}(\chi), \tag{43}$$

where singular values σ are arranged in descending order to ensure that the energy-intensive modes are prioritized. Figure 15(a) shows the time evolution of amplitude for the first three POD modes. These modes are ranked according to their energy (singular value) as shown in Fig. 15(b). M2 and M3 correspond to the inherent FM and EM of the VIV system. M2 is the only unstable mode before control and has an obvious increase for two periods of oscillation after control, which contributes to the transition growth.
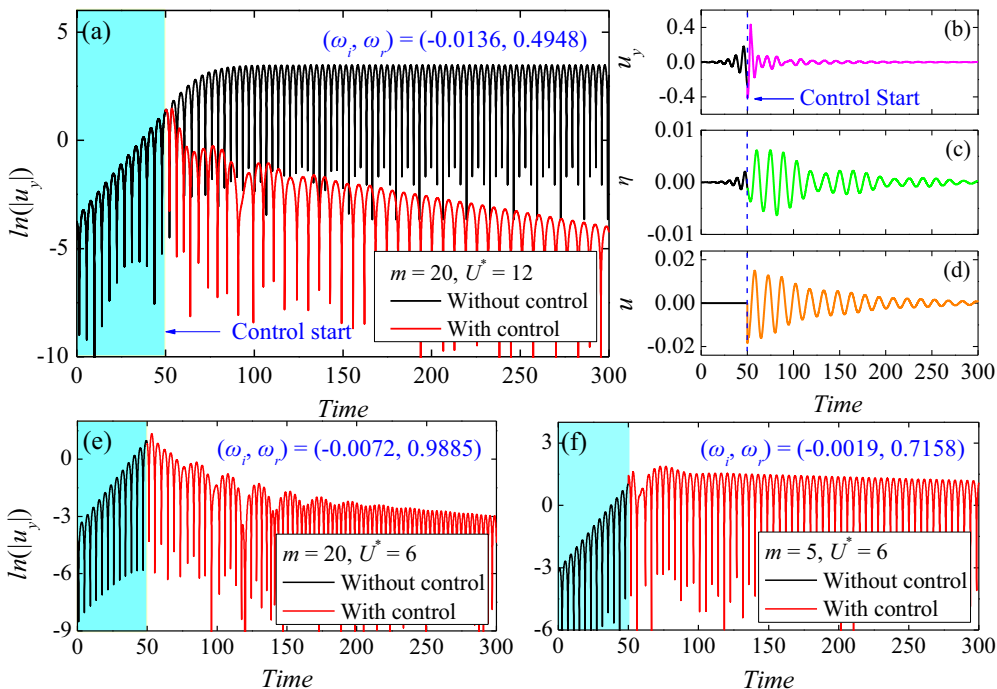
FIG. 14. (a) Flow response at the probe location with and without control for $(m, U^*) = (20, 12)$, revealing an increase rate of $\omega_i = -0.0136$ and an angular frequency of $\omega_r = 0.4948$ during the asymptotic phase; (b) measurement u_y; (c) normal displacement y of the cylinder; (d) control action u; (e) the control performance for $(m, U^*) = (20, 6)$, revealing $(\omega_i, \omega_r) = (-0.0072, 0.9885)$; and (f) the control performance for $(m, U^*) = (5, 6)$, revealing $(\omega_i, \omega_r) = (-0.0019, 0.7158)$.

To gain deeper insights into the effectiveness of control within both the FOM and ROM systems, we carry out a comprehensive comparative analysis of their respective eigenvalues. Table II presents a comparison between the eigenvalues of the FOM system after being controlled by the LQG controller and those of the ROM system (i.e., the leading modes in Fig. 13). It is evident that, for the two cases with $m = 20$, the decrease rates of the eigenmode for the FOM are $\omega_i = -0.0136$ and -0.0072, which are close to those for the ROM, i.e., $\omega_i = -0.0119$ and -0.0063. This indicates that the postcontrol states of both the FOM and ROM systems show similarities when the mass ratio
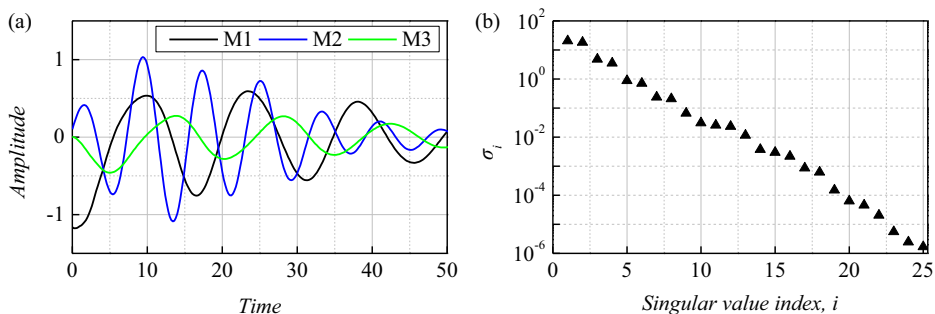

FIG. 15. (a) Time evolution of the first three POD modes. M1, M2, and M3 represent the first, second, and third POD mode, respectively. (b) The first 25 singular values.

TABLE II. Eigenvalues, wavelength, and wave speed for precontrol cases (pre) and postcontrol cases (post). In controlled cases, the LQG controller is applied to control the FOM system. The last column gives leading eigenvalues of the ROM after control shown in Fig. 13.

(m, U^*)	FOM (pre)	λ (pre)	v_t (pre)	FOM (post)	λ (post)	v_t (post)	ROM
$(20, 12)$	$0.0995 \pm 0.7402i$	6.19	0.729	$-0.0136 \pm 0.4848i$	10.21	0.786	$-0.0119 \pm 0.4159i$
$(20, 6)$	$0.0926 \pm 0.7475i$	6.07	0.722	$-0.0072 \pm 0.9885i$	4.41	0.692	$-0.0063 \pm 0.9762i$
$(5, 6)$	$0.0825 \pm 0.7664i$	5.95	0.726	$-0.0019 \pm 0.7158i$	6.68	0.761	$-0.0051 \pm 0.7904i$

is large. However, for small mass ratio ($m = 5$), there is a substantial disparity in the decrease rates of both systems. This divergence may be attributed to the weak control robustness, as discussed in Sec. IV C. Another interesting observation is the significant variation in frequencies before and after control across these three cases. There is a minor difference (maximum relative error of about 15%) in frequencies before control, whereas there is a substantial distinction in the magnitude of frequencies after control. We further explain this phenomenon with the spatial distribution of eigenfunctions.

Figure 16 compares the vorticity contours of the flow before and after control for three test cases. Significant differences in vorticity pattern are evident. For the state without control, a similar staggered streamwise-traveling pattern can be observed across all three cases. The values of the wavelength λ, defined as the distance between adjacent positive and negative vortices within the $x \in (10, 20)$ range, are nearly identical. After control, the vorticity patterns undergo a dramatic transformation, as well as their wavelengths. Among the three cases, the perturbation region, that is, the region with high perturbation vorticity, transitions closer to the cylinder for shorter wavelengths and transitions downstream for longer wavelengths. However, the speed of the traveling waves, defined as $v_t = \omega_r \times \lambda$, undergoes only minor variations, as detailed in Table II. Moreover, the patterns observed in the controlled flow can be correlated with intrinsic eigenmodes obtained from the global instability analysis in Fig. 17. For the case with $m = 20$, the controlled modes (solutions after control) exhibit similarities to the elastic mode, where the contour in Fig. 16(b) closely resembles the global eigenmodes shown in Fig. 17(a). However, results diverge in the case of $(m, U^*) = (5, 6)$, where none of the stable eigenmodes closely resembles the controlled modes. A new mode is created, which shares a pattern similar to that of the FEM-II mode for the case $(m, U^*) = (5, 7)$ in Fig. 17(b). Inducing the new mode appears to be more difficult than modifying
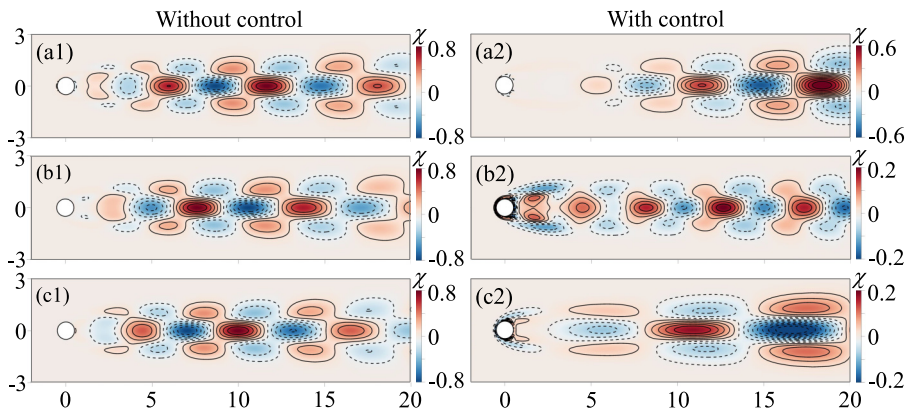

FIG. 16. Vorticity contours of states without control (left) and with control (right) for (a) $(m, U^*) = (5, 6)$, (b) $(m, U^*) = (20, 6)$, (c) $(m, U^*) = (20, 12)$. Without-control snapshots are captured at $t = 50$, while with-control snapshots are taken at $t = 250$ (i.e., within the asymptotic decay phase).
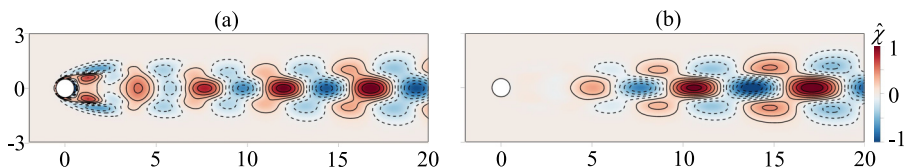
FIG. 17. (a) Eigenfunction (normalized vorticity field $\hat{\chi}$) of the EM with $(m, U^*) = (20, 6.0)$; (b) eigenfunction for FEM-II with $(m, U^*) = (5, 7.0)$.

the existing modes, leading to worse control performance for $(m, U^*) = (5, 6)$ when compared to the case with $m = 20$.

Finally, we test the robustness of the control strategy on a range of Reynolds number. Based on the discussion of selection of control parameters and actuator and probe placement, we select a control strategy at Re = 80, with $(m, U^*) = (20, 12)$, and specific control parameters $(R, G) = (10^{-3}, 10^2)$ as our focal case. Figure 18(a) shows the resulting increase rate ω_i after implementing this strategy to control the FOM system under varying Reynolds numbers. It is expected that ω_i increases with the Reynolds number. It becomes evident that $\text{Re}_c \approx 92.5$ serves as the upper limit of the Reynolds number range for which the control strategy is effective. Beyond this threshold, such as Re = 95 and 100, the flow becomes uncontrollable. Nevertheless, it is noteworthy that, even at these higher Reynolds numbers, the increase rates remain lower than those in uncontrolled cases, suggesting that this control strategy can still delay VIV under these challenging conditions.

To validate the robustness of above control strategy, we evaluate the practical performance of the off-design controller for two specific Reynolds numbers, Re = 60 (case A) and Re = 90 (case B). In addition, we apply the same random initial condition to both cases to assess the controller's robustness across different initial conditions. Figure 18(b) shows the time evolution of the cylinder's displacement under control for cases A and B. It is evident that the controller successfully controls the VIV in both cases. To distinguish between different frequency regimes, we segment the time series into two stages: Stage-I (where cases A and B exhibit nearly identical frequencies) occurring at $t < 100$, and Stage-II (with case A having a lower frequency at $\omega_r = 0.5027$ compared to case

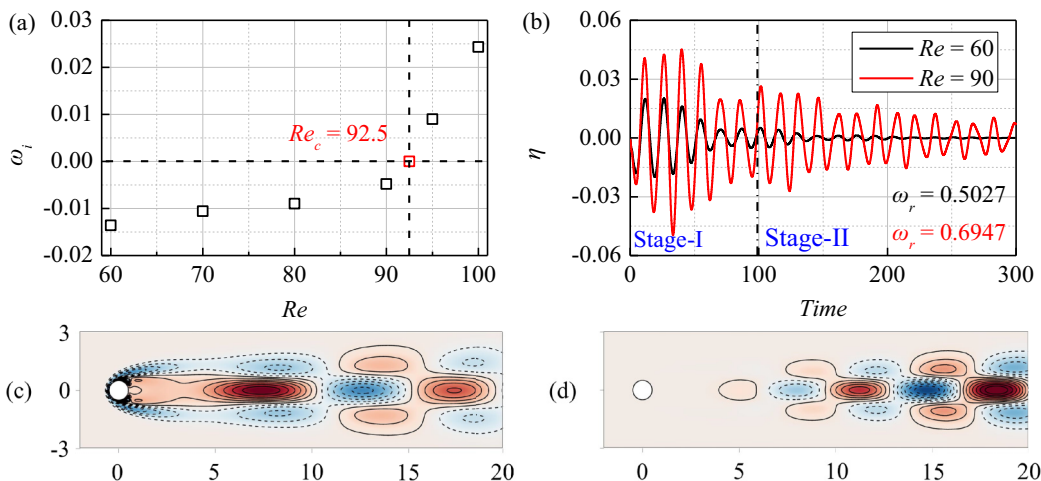FIG. 18. (a) Asymptotic increase rate for different Reynolds numbers while maintaining the same $(m, U^*) = (20, 12)$ using control strategy at Re = 80, with control parameters $(R, G) = (10^{-3}, 10^2)$. (b) Comparison of displacement of cylinder for Re = 60 (referred to as case A) and Re = 90 (referred to as case B). Contours of vorticity for (c) case A and (d) case B at $t = 300$, respectively.

B at $\omega_r = 0.6947$) unfolding at $t > 100$. It is worth noting that the initial conditions exert their influence primarily during Stage-I. For a comprehensive view of Stage-II (asymptotic phases), we can refer to the vorticity contours presented in Figs. 18(c) and 18(d) at $t = 300$.

V. CONCLUSION

In this work, we develop a reduced-order model-based feedback control strategy to suppress the vortex-induced vibration (VIV) of a spring-mounted cylinder. To do this, we first derive the linear adjoint equation of the fluid-structure coupled system. Then, we develop a reduced-order model (ROM) based on the balanced proper orthogonal decomposition (BPOD) method. A comprehensive global linear instability analysis on this VIV system is conducted, considering a wide range of parameters, including Reynolds number Re, mass ratio m, and reduced speed U^*. The obtained physical insights significantly enhance our understanding of the transition from eigenmodes during the processes of instability and control, and help to elucidate the control mechanism. By comparing with the full-order model (FOM) technique, we prove that the projection-free snapshot-based BPOD modeling method is suited for this VIV problem. Next, we develop an active flow control (AFC) strategy based on this ROM to control jets of a pair of blowing and suction actuators attached to the cylinder for suppressing VIV and stabilizing wake flow of the FOM. Optimal control strategies obtained by using the LQG algorithm can successfully control the VIV system up to a Reynolds number of Re = 100.

Several interesting findings have emerged from the analysis of the controlled flow. We have observed that the wavemaker regions are not the ideal position to place velocity probes for the VIV system. Additionally, the angle of actuators exhibits only a weak influence on controlled robustness. Through our investigation, we have identified that positioning probes near $x = 3.0$ yields a high stability margin across various Reynolds numbers, all while maintaining controllability. This strategic placement minimizes time lag and allows for the effective measurement of unstable mode development downstream. The controller mainly adjusts or eliminates unstable eigenmodes. We have observed that the unstable elastic mode has been modified to a stable mode for $m = 20$ and a new stable mode has been generated for $m = 5$. The former occurs when there are inherent eigenmodes close to the zero growth rate plane, resulting in effective control performance that aligns with the predicted outcome. However, for the latter, it may require additional energy input into the system to sustain these new modes, potentially leading to outcomes that fall short of expectations.

Overall, the current work provides a valuable ROM applicable to fluid-structure interaction problems. The significance of developing this grey-box model is further evident in its capacity to enhance interpretability and shed light on control strategy for black-box models.

APPENDIX A: DERIVATION OF ADJOINT EQUATIONS

The adjoint equations are derived from the linearized equations (13)–(17) under the inner product defined as the integral over the domain Ω and time horizon T_0:

$$\langle \boldsymbol{q}^{\dagger}, \boldsymbol{q}' \rangle = \int_{T_0} \int_{\Omega} (\boldsymbol{q}^{\dagger})^T \boldsymbol{q}' d\Omega dt. \tag{A1}$$

In the context of VIV, $\boldsymbol{L}'$ represents the linearized VIV equations defined by Eqs. (13)–(17) and $\boldsymbol{L}^{\dagger}$ represents the adjoint operator satisfying the Lagrange identity under the inner product defined

in Eq. (A1),

$$\langle \boldsymbol{L}^{\dagger}\boldsymbol{q}^{\dagger}, \boldsymbol{q}' \rangle = \langle \boldsymbol{q}^{\dagger}, \boldsymbol{L}'\boldsymbol{q}' \rangle. \tag{A2}$$

The direct and adjoint state vectors are defined as $\boldsymbol{q}' = (\boldsymbol{u}', p', \eta', \zeta', \xi')^{T}$, which lies in the domain of $\boldsymbol{L}'$, and $\boldsymbol{q}^{\dagger} = (\boldsymbol{u}^{\dagger}, p^{\dagger}, \eta^{\dagger}, \zeta^{\dagger}, \xi^{\dagger})^{T}$, which lies in the domain of $\boldsymbol{L}^{\dagger}$. The Lagrange identity can be written as

$$\langle \boldsymbol{L}^{\dagger}\boldsymbol{q}^{\dagger}, \boldsymbol{q}' \rangle = \langle \boldsymbol{q}^{\dagger}, \boldsymbol{L}'\boldsymbol{q}' \rangle$$

$$= \begin{cases} \int_{T_0} \int_{\Omega} \boldsymbol{u}^{\dagger} \big[\frac{\partial \boldsymbol{u}'}{\partial t} + (\boldsymbol{u}' \cdot \boldsymbol{\nabla})U_b + (U_b \cdot \boldsymbol{\nabla})\boldsymbol{u}' + \boldsymbol{\nabla} p' - \frac{1}{\mathrm{Re}}\nabla^2 \boldsymbol{u}' - (\zeta' \boldsymbol{n}_y \cdot \boldsymbol{\nabla})U_b \big] d\Omega dt \\ + \int_{T_0} \int_{\Omega} p^{\dagger}(\boldsymbol{u}' \cdot \boldsymbol{\nabla})d\Omega dt + \int_{T_0} \eta^{\dagger}\big(\frac{\partial \eta'}{\partial t} - \zeta'\big)dt + \int_{T_0} \zeta^{\dagger}\big(\frac{\partial \zeta'}{\partial t} - \xi'\big)dt \\ + \int_{T_0} \xi^{\dagger}\big\{\xi' + \frac{4\pi \gamma}{U^*}\zeta' + \big(\frac{2\pi}{U^*}\big)^2 \eta' - \frac{4}{\pi m}[\boldsymbol{F}_p(p') + \boldsymbol{F}_u(\boldsymbol{u}')]\big\}dt. \end{cases} \tag{A3}$$

After integrating by parts and using the divergence theorem, we can obtain Eq. (A4) from Eq. (A3),

$$\Rightarrow \begin{cases} \underbrace{\int_{T_0} \int_{\Omega} \big\{ \boldsymbol{u}' \big[-\frac{\partial \boldsymbol{u}^{\dagger}}{\partial t} - \boldsymbol{\nabla}\boldsymbol{u}^{\dagger} \cdot U_b + (\boldsymbol{\nabla}U_b)^T \cdot \boldsymbol{u}^{\dagger} + \boldsymbol{\nabla}p^{\dagger} - \frac{1}{\mathrm{Re}}\nabla^2\boldsymbol{u}^{\dagger} - \frac{4}{\pi m}\boldsymbol{F}_u \zeta^{\dagger} \big] \big\}d\Omega dt}_{\text{term1}} \\ \underbrace{\int_{T_0} \int_{\Omega} \big[p'\big(\boldsymbol{\nabla} \cdot \boldsymbol{u}^{\dagger} - \frac{4}{\pi m}\boldsymbol{F}_p \zeta^{\dagger}\big) \big]d\Omega dt}_{\text{term2}} + \underbrace{\int_{T_0} \big[\eta'\big(-\frac{\partial \eta^{\dagger}}{\partial t} + \big(\frac{2\pi}{U^*}\big)^2 \xi^{\dagger}\big) \big]dt}_{\text{term3}} \\ + \underbrace{\int_{T_0} \big\{ \zeta'\big[-\boldsymbol{n}_y(\boldsymbol{\nabla}\boldsymbol{u}^{\dagger} \cdot U_b) - \eta^{\dagger} - \frac{\partial \zeta^{\dagger}}{\partial t} + \frac{4\pi \gamma}{U^*}\xi^{\dagger} \big] + \xi'(-\zeta^{\dagger} + \xi^{\dagger}) \big\}dt}_{\text{term4}} \\ + \underbrace{\int_{T_0} \oint_{\Gamma} (\boldsymbol{u}'\boldsymbol{u}^{\dagger}U_b + \boldsymbol{u}'\boldsymbol{\sigma}^{\dagger} - \boldsymbol{u}^{\dagger}\boldsymbol{\sigma}') \cdot \boldsymbol{n} d\Gamma dt}_{\text{term5}} + \underbrace{\big[\int_{\Omega} (\boldsymbol{u}'\boldsymbol{u}^{\dagger})d\Omega + \frac{d(\eta'\eta^{\dagger})}{dt} + \frac{d(\zeta'\zeta^{\dagger})}{dt} \big]_0^{T_0}}_{\text{term6}}, \end{cases} \tag{A4}$$

in which the direct and adjoint forces are denoted in compact notations given by

$$\boldsymbol{\sigma}' = -p'\boldsymbol{n} + \frac{1}{\mathrm{Re}}[\boldsymbol{\nabla}\boldsymbol{u}' + (\boldsymbol{\nabla}\boldsymbol{u}')^T],$$

$$\boldsymbol{\sigma}^{\dagger} = -p^{\dagger}\boldsymbol{n} + \frac{1}{\mathrm{Re}}[\boldsymbol{\nabla}\boldsymbol{u}^{\dagger} + (\boldsymbol{\nabla}\boldsymbol{u}^{\dagger})^T]. \tag{A5}$$

Due to operators $\boldsymbol{L}'$ and $\boldsymbol{L}^{\dagger}$ satisfying

$$\boldsymbol{L}(t)\boldsymbol{q}'(t_0) = \boldsymbol{q}'(t_0 + t), \quad \boldsymbol{L}^{\dagger}(t)\boldsymbol{q}^{\dagger}(t_0) = \boldsymbol{q}^{\dagger}(t_0 - t), \tag{A6}$$

the first term in term 6 can be rewritten as

$$\int_{\Omega} \boldsymbol{u}'(T_0)\boldsymbol{u}^{\dagger}(T_0)d\Omega = \langle \boldsymbol{L}'(T_0)\boldsymbol{u}'(0), \boldsymbol{u}^{\dagger}(T_0) \rangle = \langle \boldsymbol{u}'(0), \boldsymbol{L}^{\dagger}(T_0)\boldsymbol{u}^{\dagger}(T_0) \rangle = \int_{\Omega} \boldsymbol{u}'(0)\boldsymbol{u}^{\dagger}(0)d\Omega. \tag{A7}$$

The same result holds true for the second and third terms of term 6. Then, term 6 becomes

$$\big[\int_{\Omega} (\boldsymbol{u}'\boldsymbol{u}^{\dagger})d\Omega + \frac{d(\eta'\eta^{\dagger})}{dt} + \frac{d(\zeta'\zeta^{\dagger})}{dt} \big]_0^{T_0}$$

$$= \int_{\Omega} (\boldsymbol{u}'(T_0)\boldsymbol{u}^{\dagger}(T_0))d\Omega + \frac{d(\eta'(T_0)\eta^{\dagger}(T_0))}{dt} + \frac{d(\zeta'(T_0)\zeta^{\dagger}(T_0))}{dt}$$

$$- \int_{\Omega} (\boldsymbol{u}'(0)\boldsymbol{u}^{\dagger}(0))d\Omega + \frac{d(\eta'(0)\eta^{\dagger}(0))}{dt} + \frac{d(\zeta'(0)\zeta^{\dagger}(0))}{dt} = 0. \tag{A8}$$
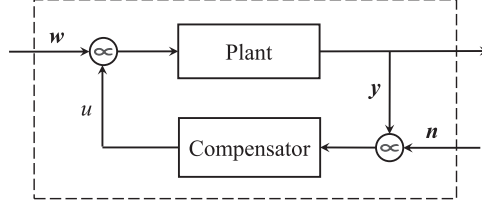
FIG. 19. Block diagram of the feedback control framework.

We obtain the adjoint equations by requiring terms 1–4 to be zero with boundary conditions by requiring term 5 to be zero [60]. So, the final set of adjoint equations for the FSI of a 2D oscillating cylinder can be written as

$$\boldsymbol{\nabla} \cdot \boldsymbol{u}^\dagger - \frac{4}{\pi m} \boldsymbol{F}_p \xi^\dagger = 0, \tag{A9}$$

$$-\frac{\partial \boldsymbol{u}^\dagger}{\partial t} - \boldsymbol{\nabla} \boldsymbol{u}^\dagger \cdot U_b + (\boldsymbol{\nabla} U_b)^T \cdot \boldsymbol{u}^\dagger + \boldsymbol{\nabla} p^\dagger - \frac{1}{\mathrm{Re}} \nabla^2 \boldsymbol{u}^\dagger - \frac{4}{\pi m} \boldsymbol{F}_u \xi^\dagger = 0, \tag{A10}$$

$$-\frac{\partial \eta^\dagger}{\partial t} + \left(\frac{2\pi}{U^*}\right)^2 \xi^\dagger = 0, \tag{A11}$$

$$-\frac{\partial \zeta^\dagger}{\partial t} - \boldsymbol{n}_y \cdot (\boldsymbol{\nabla} U_b)^T \cdot \boldsymbol{u}^\dagger - \eta^\dagger + \frac{4\pi \gamma}{U^*} \xi^\dagger = 0, \tag{A12}$$

$$\xi^\dagger - \zeta^\dagger = 0. \tag{A13}$$

For the outer boundaries of the domain, the boundary terms (term 5) can be written compactly as

$$\int_T \oint_\Gamma [\boldsymbol{u}'(\boldsymbol{u}^\dagger U_b + \boldsymbol{\sigma}^\dagger) - \boldsymbol{u}^\dagger \boldsymbol{\sigma}'] \cdot \boldsymbol{n} d\Gamma dt = 0. \tag{A14}$$

Considering homogeneous Dirichlet and stress-free conditions for the linear direct problem, the boundary conditions for the adjoints reduce to

$$\boldsymbol{u}^\dagger = \boldsymbol{u}' \quad \text{on } \Gamma_{cy},$$

$$\boldsymbol{u}^\dagger = 0 \quad \text{on } \Gamma_{\mathrm{in}} \cup \Gamma_{\mathrm{top}} \cup \Gamma_{\mathrm{bottom}},$$

$$(\boldsymbol{\sigma}^\dagger + \boldsymbol{u}^\dagger U_b) \cdot \boldsymbol{n} = 0 \quad \text{on } \Gamma_{\mathrm{out}}. \tag{A15}$$

APPENDIX B: FEEDBACK CONTROLLER DESIGN

We design a full-state information controller based on the reduced-order model using the LQG framework [62]. The control block diagram, depicted in Fig. 19, comprises the true flow plant, the closed-loop regulator, and $(u, \boldsymbol{y})$ representing the control and measurement signals, respectively. This configuration also accounts for the presence of noise $\boldsymbol{n}$ and disturbance $\boldsymbol{w}$.

Normalized disturbance inputs $\boldsymbol{n}'$ and $\boldsymbol{w}'$, with $\boldsymbol{n} = \sqrt{N}\boldsymbol{n}'$ and $\boldsymbol{w} = \sqrt{W}\boldsymbol{w}'$, where $N = \langle \boldsymbol{n}^T, \boldsymbol{n} \rangle$ and $W = \langle \boldsymbol{w}^T, \boldsymbol{w} \rangle$, are introduced to denote covariances of probe noise and controller-added noise. Then, we obtained the reduced-order compensated system:

$$\bar{N}\frac{d\bar{\boldsymbol{q}}'}{dt} = \bar{M}'\bar{\boldsymbol{q}}' + \bar{B}u + \sqrt{W}\bar{B}\boldsymbol{w}', \tag{B1}$$

$$\bar{y} = \bar{C}\bar{\boldsymbol{q}}' + \sqrt{N}\boldsymbol{n}', \tag{B2}$$

where variables with an overbar represent the reduced system. The objective function is defined as

$$H = \langle \bar{\boldsymbol{q}}'^T \bar{C}^T \bar{C} \bar{\boldsymbol{q}}' + l^2 u^2 \rangle, \tag{B3}$$

where l^2 is the control cost. The LQG controller works to minimize the expected value of H. The compensator can be written in a state-space form according to

$$\bar{N}\frac{d\tilde{\boldsymbol{q}}'}{dt} = \boldsymbol{J}\tilde{\boldsymbol{q}}' + \boldsymbol{L}\bar{y}, \tag{B4}$$

$$u = \boldsymbol{K}\tilde{\boldsymbol{q}}', \tag{B5}$$

where $\tilde{\boldsymbol{q}}'$ is the estimated coefficient vector approximating $\bar{\boldsymbol{q}}'$; $\boldsymbol{L}$ and $\boldsymbol{K}$ are the Kalman and control gains, which are determined by solving two algebraic matrix Riccati equations as [62]

$$\bar{\boldsymbol{M}}'^T \boldsymbol{R} + \boldsymbol{R}\bar{\boldsymbol{M}}' - \frac{\boldsymbol{R}\bar{\boldsymbol{B}}\bar{\boldsymbol{B}}^T \boldsymbol{R}}{l^2} + \bar{\boldsymbol{C}}^T\bar{\boldsymbol{C}} = 0, \tag{B6}$$

$$\bar{\boldsymbol{M}}'\boldsymbol{S} + \boldsymbol{S}\bar{\boldsymbol{M}}'^T - \frac{\boldsymbol{S}\bar{\boldsymbol{C}}^T\bar{\boldsymbol{C}}\boldsymbol{S}}{E} + \bar{\boldsymbol{B}}F\bar{\boldsymbol{B}}^T = 0, \tag{B7}$$

where $\boldsymbol{R}$ and $\boldsymbol{S}$ are solutions of Eqs. (B6) and (B7), respectively. Control gain $\boldsymbol{K}$ and Kalman gain $\boldsymbol{L}$ are defined as

$$\boldsymbol{K} = -\frac{\bar{\boldsymbol{B}}^T \boldsymbol{R}}{l^2}, \tag{B8}$$

$$\boldsymbol{L} = \frac{\boldsymbol{S}\bar{\boldsymbol{C}}^T}{E}, \tag{B9}$$

where $G = E/F$ and $R = l^2$ are adjustable parameters governing these two gains. Moreover, the system matrix $\boldsymbol{J}$ is obtained straightforwardly as $\boldsymbol{J} = \bar{\boldsymbol{M}}' - \boldsymbol{L}\bar{\boldsymbol{C}} + \bar{\boldsymbol{B}}\boldsymbol{K}$. The LQG framework guarantees the stability of $\boldsymbol{J}$ while the reduced system $\bar{\boldsymbol{M}}'$ remains unstable.

---

[1] C. H. Williamson and R. Govardhan, Vortex-induced vibrations, Annu. Rev. Fluid Mech. **36**, 413 (2004).

[2] J. Simmons and P. Cleary, Measurement of aerodynamic power associated with vortex-induced vibration of electrical transmission lines, IEEE Trans. Power App. Syst. **PAS-99**, 158 (1980).

[3] J.-s. Wang, D. Fan, and K. Lin, A review on flow-induced vibration of offshore circular cylinders, J. Hydrodyn. **32**, 415 (2020).

[4] M. Schäfer, S. Turek, F. Durst, E. Krause, and R. Rannacher, *Benchmark Computations of Laminar Flow around a Cylinder* (Springer, Berlin, 1996).

[5] W. Zhang, X. Li, Z. Ye, and Y. Jiang, Mechanism of frequency lock-in in vortex-induced vibrations at low Reynolds numbers, J. Fluid Mech. **783**, 72 (2015).

[6] J. Dahl, F. Hover, M. Triantafyllou, and O. Oakley, Dual resonance in vortex-induced vibrations at subcritical and supercritical Reynolds numbers, J. Fluid Mech. **643**, 395 (2010).

[7] G. S. Baarholm, C. M. Larsen, and H. Lie, On fatigue damage accumulation from in-line and cross-flow vortex-induced vibrations on risers, J. Fluids Struct. **22**, 109 (2006).

[8] C. Wang, H. Tang, S. Yu, and F. Duan, Active control of vortex-induced vibrations of a circular cylinder using windward-suction-leeward-blowing actuation, Phys. Fluids. **28**, 053601 (2016).

[9] M. Raissi, Z. Wang, M. S. Triantafyllou, and G. E. Karniadakis, Deep learning of vortex-induced vibrations, J. Fluid Mech. **861**, 119 (2019).

[10] C. Zheng, F. Xie, T. Ji, X. Zhang, Y. Lu, H. Zhou, and Y. Zheng, Data-efficient deep reinforcement learning with expert demonstration for active flow control, Phys. Fluids. **34**, 113603 (2022).

[11] B. Jin, S. J. Illingworth, and R. D. Sandberg, Feedback control of vortex shedding using a resolvent-based modelling approach, J. Fluid Mech. **897**, A26 (2020).

[12] C. W. Rowley and S. T. Dawson, Model reduction for flow analysis and control, Annu. Rev. Fluid Mech. **49**, 387 (2017).

[13] S. L. Brunton and B. R. Noack, Closed-loop turbulence control: Progress and challenges, Appl. Mech. Rev. **67**, 050801 (2015).

[14] Z. Ma, S. Ahuja, and C. W. Rowley, Reduced-order models for control of fluids using the eigensystem realization algorithm, Theor. Comput. Fluid Dyn. **25**, 233 (2011).

[15] S. L. Brunton, S. T. Dawson, and C. W. Rowley, State-space model identification and feedback control of unsteady aerodynamic forces, J. Fluids Struct. **50**, 253 (2014).

[16] T. L. B. Flinois, A. S. Morgans, and P. J. Schmid, Projection-free approximate balanced truncation of large unstable systems, Phys. Rev. E **92**, 023012 (2015).

[17] W. Yao and R. Jaiman, Feedback control of unstable flow and vortex-induced vibration using the eigensystem realization algorithm, J. Fluid Mech. **827**, 394 (2017).

[18] Z. Cheng, F.-S. Lien, E. H. Dowell, E. Yee, R. Wang, J. H. Zhang, Critical effect of fore-aft tapering on galloping triggering for a trapezoidal body, J. Fluid Mech. **967**, A18 (2023).

[19] F. Luo, C. Gao, and W. Zhang, The key to suppress vortex-induced vibration: Stability of the structural mode, J. Fluids Struct. **113**, 103692 (2022).

[20] C. W. Rowley, Model reduction for fluids, using balanced proper orthogonal decomposition, Int. J. Bifurcation Chaos **15**, 997 (2005).

[21] M. Ilak and C. W. Rowley, Modeling of transitional channel flow using balanced proper orthogonal decomposition, Phys. Fluids. **20**, 034103 (2008).

[22] S. G. Siegel, J. Seidel, C. Fagley, D. Luchtenburg, K. Cohen, and T. McLaughlin, Low-dimensional modelling of a transient cylinder wake using double proper orthogonal decomposition, J. Fluid Mech. **610**, 1 (2008).

[23] S. Ahuja and C. W. Rowley, Feedback control of unstable steady states of flow past a flat plate using reduced-order estimators, J. Fluid Mech. **645**, 447 (2010).

[24] O. Semeraro, S. Bagheri, L. Brandt, and D. S. Henningson, Feedback control of three-dimensional optimal disturbances using reduced-order models, J. Fluid Mech. **677**, 63 (2011).

[25] L. Von Rueden, S. Mayer, K. Beckh, B. Georgiev, S. Giesselbach, R. Heese, B. Kirsch, J. Pfrommer, A. Pick, R. Ramamurthy, M. Walczak, J. Garcke, C. Bauckhage, and J. Schuecker, Informed machine learning—a taxonomy and survey of integrating prior knowledge into learning systems, IEEE Trans. Knowl. Data Eng. **35**, 614 (2021).

[26] K. Taira, S. L. Brunton, S. T. Dawson, C. W. Rowley, T. Colonius, B. J. McKeon, O. T. Schmidt, S. Gordeyev, V. Theofilis, and L. S. Ukeiley, Modal analysis of fluid flows: An overview, AIAA J. **55**, 4013 (2017).

[27] M. Lesoinne, M. Sarkis, U. Hetmaniuk, and C. Farhat, A linearized method for the frequency analysis of three-dimensional fluid/structure interaction problems in all flow regimes, Comput. Methods Appl. Mech. Eng. **190**, 3121 (2001).

[28] P. S. Negi, A. Hanifi, and D. S. Henningson, On the linear global stability analysis of rigid-body motion fluid–structure-interaction problems, J. Fluid Mech. **903**, A35 (2020).

[29] M. Á. Fernández and P. Le Tallec, Linear stability analysis in fluid–structure interaction with transpiration. Part II: Numerical analysis and applications, Comput. Methods Appl. Mech. Eng. **192**, 4837 (2003).

[30] J.-L. Pfister, O. Marquet, and M. Carini, Linear stability analysis of strongly coupled fluid–structure problems with the arbitrary-Lagrangian–Eulerian method, Comput. Methods Appl. Mech. Eng. **355**, 663 (2019).

[31] A. Goza, T. Colonius, and J. E. Sader, Global modes and nonlinear analysis of inverted-flag flapping, J. Fluid Mech. **857**, 312 (2018).

[32] S. Cao, A. Main, and K. G. Wang, Robin-Neumann transmission conditions for fluid-structure coupling: Embedded boundary implementation and parameter analysis, Int. J. Numer. Methods Eng. **115**, 578 (2018).

[33] S. Cao, G. Wang, and K. G. Wang, A spatially varying Robin interface condition for fluid-structure coupled simulations, Int. J. Numer. Methods Eng. **122**, 5176 (2021).

[34] H.-K. Jiang, K. Luo, Z.-Y. Zhang, J. Wu, and H.-L. Yi, Global linear instability analysis of thermal convective flow using the linearized lattice Boltzmann method, J. Fluid Mech. **944**, A31 (2022).

[35] H.-K. Jiang, Y. Zhang, Z.-Y. Zhang, K. Luo, and H.-L. Yi, Instability and bifurcations of electro-thermo-convection in a tilted square cavity filled with dielectric liquid, Phys. Fluids **34**, 064116 (2022).

[36] R. Basso, Y. Hwang, G. Assi, and S. Sherwin, Instabilities and sensitivities in a flow over a rotationally flexible cylinder with a rigid splitter plate, J. Fluid Mech. **928**, A24 (2021).

[37] J. Tchoufag, D. Fabre, and J. Magnaudet, Global linear stability analysis of the wake and path of buoyancy-driven disks and thin cylinders, J. Fluid Mech. **740**, 278 (2014).

[38] D. Sabino, D. Fabre, J. Leontini, and D. L. Jacono, Vortex-induced vibration prediction via an impedance criterion, J. Fluid Mech. **890**, A4 (2020).

[39] P. J. Schmid and L. Brandt, Analysis of fluid systems: Stability, receptivity, sensitivity: Lecture notes from the Flow-Nordita Summer School on Advanced Instability Methods for Complex Flows, Stockholm, Sweden, 2013, Appl. Mech. Rev. **66**, 024803 (2014).

[40] E. Åkervik, J. Hœpffner, U. Ehrenstein, and D. S. Henningson, Optimal growth, model reduction and control in a separated boundary-layer flow using global eigenmodes, J. Fluid Mech. **579**, 305 (2007).

[41] T. L. Flinois and A. S. Morgans, Feedback control of unstable flows: A direct modelling approach using the eigensystem realisation algorithm, J. Fluid Mech. **793**, 41 (2016).

[42] J. Li and M. Zhang, Reinforcement-learning-based control of confined cylinder wakes with stability analyses, J. Fluid Mech. **932**, A44 (2022).

[43] K. K. Chen and C. W. Rowley, H_2 optimal actuator and sensor placement in the linearised complex Ginzburg–Landau system, J. Fluid Mech. **681**, 241 (2011).

[44] S. F. Oehler and S. J. Illingworth, Sensor and actuator placement trade-offs for a linear model of spatially developing flows, J. Fluid Mech. **854**, 34 (2018).

[45] A. Barbagallo, D. Sipp, and P. J. Schmid, Closed-loop control of an open cavity flow using reduced-order models, J. Fluid Mech. **641**, 1 (2009).

[46] S. J. Illingworth, A. S. Morgans, and C. W. Rowley, Feedback control of cavity flow oscillations using simple linear models, J. Fluid Mech. **709**, 223 (2012).

[47] N. Fabbiane, B. Simon, F. Fischer, S. Grundmann, S. Bagheri, and D. S. Henningson, On the role of adaptivity for robust laminar flow control, J. Fluid Mech. **767**, R1 (2015).

[48] J. C. Doyle, Guaranteed margins for LQG regulators, IEEE Trans. Autom. Control. **23**, 756 (1978).

[49] A. Barbagallo, G. Dergham, D. Sipp, P. J. Schmid, and J.-C. Robinet, Closed-loop control of unsteadiness over a rounded backward-facing step, J. Fluid Mech. **703**, 326 (2012).

[50] D. Sipp and P. J. Schmid, Linear closed-loop control of fluid instabilities and noise-induced perturbations: A review of approaches and tools, Appl. Mech. Rev. **68**, 020801 (2016).

[51] S. J. Illingworth, Model-based control of vortex shedding at low Reynolds numbers, Theor. Comput. Fluid Dyn. **30**, 429 (2016).

[52] G. Mougin and J. Magnaudet, The generalized Kirchhoff equations and their application to the interaction between a rigid body and an arbitrary time-dependent viscous flow, Int. J. Multiphase Flow **28**, 1837 (2002).

[53] D. Z. Huang, M. J. Zahr, and P.-O. Persson, A high-order partitioned solver for general multiphysics problems and its applications in optimization, in *AIAA Scitech 2019 Forum* (AIAA, Reston, VA, 2019), p. 1697.

[54] B. Moore, Principal component analysis in linear systems: Controllability, observability, and model reduction, IEEE Trans. Autom. Control. **26**, 17 (1981).

[55] A. C. Antoulas, *Approximation of Large-Scale Dynamical Systems* (SIAM, Philadelphia, 2005).

[56] F. Hecht, New development in FreeFEM++, J. Numer. Math. **20**, 251 (2012).

[57] R. B. Lehoucq, D. C. Sorensen, and C. Yang, *ARPACK Users' Guide: Solution of Large-Scale Eigenvalue Problems with Implicitly Restarted Arnoldi Methods* (SIAM, Philadelphia, 1998).

[58] N. Navrose and S. Mittal, Lock-in in vortex-induced vibration, J. Fluid Mech. **794**, 565 (2016).

[59] P. Meliga and J.-M. Chomaz, An asymptotic expansion for the vortex-induced vibrations of a circular cylinder, J. Fluid Mech. **671**, 137 (2011).

[60] S. Bagheri, L. Brandt, and D. S. Henningson, Input–output analysis, model reduction and control of the flat-plate boundary layer, J. Fluid Mech. **620**, 263 (2009).

[61] L. Sirovich, Turbulence and the dynamics of coherent structures, parts I, II and III, Q. Appl. Math. **45**, 561 (1987).

[62] B. D. Anderson and J. B. Moore, *Optimal Control: Linear Quadratic Methods* (Courier Corporation, North Chelmsford, MA, 2007).